

Order of Magnitude Analysis and Data-Based Physics-Informed Symbolic Regression for Turbulent Pipe Flow

Yunus Emre Ünal and Özgür Ertunç*

Fluid Dynamics and Spray Laboratory, Mechanical Engineering Department, Özyegin University, Istanbul, Türkiye

Ismail Ari

Cloud Computing Research Laboratory, Computer Science Department, Özyegin University, Istanbul, Türkiye

Ivan Otić

*Institute for Thermal Energy Technology and Safety,
Karlsruhe Institute of Technology, Karlsruhe, Germany*

(Dated: February 20, 2026)

Friction losses in rough pipes are commonly predicted with semi-empirical correlations such as the Colebrook–White equation [C. F. Colebrook, *J. Inst. Civ. Eng.* 11, 133 (1939)] and explicit approximations (e.g. Haaland) [S. E. Haaland, *J. Fluids Eng.* 105, 89 (1983)], which interpolate decades of data but do not fully reproduce the behaviour of Nikuradse’s rough pipe experiments [J. Nikuradse, *NACA Tech. Memo.* 1292 (1950)]. Here, we derive scaling relations for the viscous and turbulent contributions to the streamwise pressure drop using an order-of-magnitude analysis (OMA) of the Reynolds-averaged Navier-Stokes equations and the mean/turbulent kinetic-energy transport. These relations yield four quantitative physical constraints that bound the local sensitivities of ΔP to mean velocity, roughness, viscosity and density through exponent envelopes, and serve as a physics prior for symbolic regression. Using the combined data of Nikuradse and smooth-pipe measurements [M. V. Zagarola and A. J. Smits, *Phys. Rev. Lett.* 80, 239 (1998)], we seek compact and explicit correlations for $f = g(Re, \varepsilon/D)$ that fit the experiments while respecting the OMA constraints and recovering correct smooth and fully rough asymptotics rather than simply tuning another empirical interpolation between smooth-wall and fully rough limits. We modify a multigene genetic-programming engine (GPTIPS2) to jointly optimize tree structure, linear gene weights and embedded constants, and evaluate each model by three minimization objectives: fitness, structural complexity and a physics score measuring constraint violation; a three-dimensional Pareto front is evolved rather than a single regularized loss. The method discovers short, interpretable expressions that satisfy the constraints while accurately reproducing friction factors across smooth-to-rough and over a wide Reynolds number range. The best fitting correlation is validated on rough, high- Re campaigns [C. J. Swanson *et al.*, *J. Fluid Mech.* 461, 51 (2002); M. A. Shockling *et al.*, *J. Fluid Mech.* 564, 267 (2006); L. I. Langelandsvik *et al.*, *J. Fluid Mech.* 595, 323 (2008)] up to $Re \sim 10^7$. The framework generalizes to other nondimensional correlation problems where only leading-order balances are known.

I. INTRODUCTION

Predictive correlations for frictional pressure loss in pipe flows are central to hydraulic design, flow metering, and energy systems. Classical treatments express the Darcy–Weisbach friction factor f as a function of the Reynolds number Re and the relative roughness ε/D , and summarize decades of experiments in compact formulas such as the Colebrook–White equation and its explicit approximations such as Haaland equation, together with the Moody diagram that engineers use in practice [1–4]. The underlying structure is inherently dimensionless: once the flow is fully developed, the pressure gradient can depend only on the ratios of inertial to viscous forces and on the relative wall-roughness.

Dimensional analysis provides a natural starting point for such problems. Buckingham-II theorem guarantees

that any physically admissible relation among ΔP , \bar{U}_m , ρ , μ , D , L , and ε may be written in terms of a reduced set of dimensionless groups [5, 6]. For internal flows, this leads to the familiar choice of the Reynolds number and the relative roughness, so that $f = f(Re, \varepsilon/D)$. However, the theorem is silent on which dimensionless groups are most predictive and on how they should be combined. Historically, this ranking has been supplied by physical reasoning and experiments: Blasius used smooth-pipe data to infer a nearly power-law dependence of the friction factor on Re [7], while Nikuradse’s sand-grain roughness experiments mapped out the dependence on ε/D and extended the data into the fully rough regime [8]. At the same time, it has long been recognized that roughness morphology matters: compared with Nikuradse’s uniform sand grains, commercial pipes with broader distributions of protuberance sizes can exhibit a more gradual departure from the smooth-pipe law. In that setting, ε is most consistently interpreted as an effective (equivalent sand-grain) roughness referenced to Nikuradse-style behaviour, enabling different surface types to be compared

* ozgur.ertunc@ozyegin.edu.tr

on a common roughness scale [9]. In a similar spirit, earlier resistance formulations in hydraulics also emphasized relative roughness measures and reported weak power dependence of roughness coefficients on an absolute roughness scale [10]. Semi-empirical correlations such as Colebrook–White interpolate between these regimes but remain implicit and non-trivial to invert.

Recent years have seen growing interest in using data-driven methods to discover dimensionless groups and closure relations directly from experimental or numerical data. The "Virtual Nikuradse" model, for example, constructs a high-fidelity friction-factor surface from Nikuradse-style data via spline and polynomial fits [11]. More broadly, symbolic regression and related techniques seek analytical expressions that reproduce observed data while remaining compact and interpretable [12–15]. The GPTIPS 2 framework, in particular, provides a multi-gene genetic-programming implementation for symbolic regression in MATLAB [16], and tools such as PySR offer efficient modern solvers in Python/Julia [15]. Yet most of these applications only enforce dimensional homogeneity and perhaps simple bounds or penalties; they typically do not encode the detailed asymptotics and monotonicity properties that are known for pipe friction. As a result, purely data-driven symbolic models may match friction-factor data over the training range but exhibit unphysical behaviour when extrapolated: exponents in ΔP versus velocity may drift outside plausible ranges, pressure drop may decrease with increasing roughness in some corner of parameter space, or the dependence on viscosity and density may contradict basic momentum-balance considerations. For engineering use, such pathologies are unacceptable even if they occur in regions with sparse data.

In this work, we combine a problem-specific order-of-magnitude analysis (OMA) with physics-constrained symbolic regression to discover new correlations for the friction factor in turbulent pipe flows. Starting from a stream-wise momentum balance and energy equations in the framework of Reynolds decomposition and averaging, we derive an OMA model for the pressure drop that has separate viscous and roughness-dominated turbulent contributions. The two contributions are blended with a logistic function so that the resulting equation can reflect the transition from viscous effects-dominated smooth turbulent pipe flow to inertial turbulence-dominated rough turbulent pipe flow. Written in dimensionless form, this OMA model implies specific, testable trends for how the pressure drop behaves when one physical parameter is varied while the others are held fixed. We characterize these trends through four logarithmic sensitivities: (i) the effective velocity exponent, (ii) the roughness sensitivity, (iii) the viscous sensitivity, and (iv) the density sensitivity. Evaluated over the Nikuradse and Superpipe parameter ranges, the OMA model yields tight envelopes for these quantities.

We then embed these constraints in a modified symbolic-regression pipeline built on GPTIPS 2. The input space consists of a grid of candidate dimensionless

groups generated by Buckingham-II analysis; individuals are multi-gene expressions that linearly combine symbolic subtrees of these groups. For each candidate model, we first refit all linear gene weights and embedded constants by a two-stage procedure: ridge-regularized least squares followed by joint optimization of all constants via Nelder–Mead, using a fast evaluation of the OMA-inspired physics score. The final model is evaluated on three objectives: (i) fitness (normalised RMSE of f), (ii) a structural complexity measure, and (iii) a physics score that summarizes the worst violation of the OMA constraints. Multi-objective selection with Pareto sorting and crowding distance is applied directly to these three objective scores rather than folding physics into a single penalty term, so that accuracy, simplicity, and physical consistency can be traded explicitly.

The contributions of this paper are threefold. First, we derive an OMA model for pressure drop in rough turbulent pipes that yields quantitative, data-calibrated constraints on the local power-law exponents with respect to velocity, roughness, viscosity, and density. Second, we design a physics-informed symbolic-regression workflow that augments GPTIPS 2 with joint constant optimization and a three-objective Pareto search driven by these OMA constraints. Third, applying this framework to Nikuradse and Superpipe datasets, we obtain a compact explicit correlations for ΔP and $f(Re, \varepsilon/D)$ that match or exceed the accuracy of classical formulas while remaining consistent with the asymptotic behaviour implied by the OMA analysis.

II. METHODOLOGY

A. Derivation of Governing Equations

The symbolic regression process is, in principle, an optimization process, and the constraints of this process are derived from the order-of-magnitude analysis. The Reynolds transport equations, along with Reynolds decomposition and averaging, provide a suitable framework for turbulent flows. Without delving into the complexity of cylindrical coordinates, the analysis is conducted for an incompressible, fully developed horizontal channel flow. A control volume (CV) shown in Fig. 1a is selected from the fully developed portion of the channel having a height of h , and a width of w . The channel portion has a length of L and a width much longer than its height ($w \gg h$), so the flow is assumed to be two-dimensional. Hence, the momentum equation for this control volume can be written as:

$$\Sigma F_i = \frac{\partial}{\partial t} \int_{CV} \rho U_i dV + \int_{CS} \rho U_i U_j n_j dA \quad (1)$$

where ΣF_i is the net external force in the i -direction acting on the control volume, ρ is the fluid density, U_i is the i th component of velocity, n_j is the outward unit normal to the control surface, and dV and dA denote differential

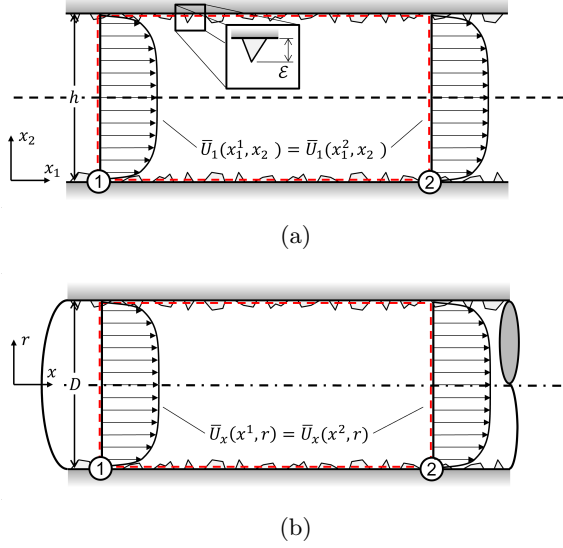


FIG. 1: Control volume (CV, red dashed region) for an incompressible fully developed turbulent statistically stationary (a) two-dimensional channel and (b) pipe flow.

volume and area elements, respectively; repeated indices imply summation.

The second term on the right-hand side (RHS) is the net flow rate of momentum, whereas the first term on the RHS is the rate of change of momentum in CV. In addition, the surface integral can be transformed into a volume integral by the divergence theorem:

$$\Sigma F_i = \frac{\partial}{\partial t} \int_{CV} \rho U_i dV + \int_{CV} \frac{\partial}{\partial x_j} \rho U_i U_j dV \quad (2)$$

To tackle the turbulence, the Reynolds decomposition is used, and all the variables, except ρ , can be written as the sum of the ensemble average and the fluctuating component:

$$\begin{aligned} \Sigma(\bar{F}_i + f_i) &= \frac{\partial}{\partial t} \int_{CV} \rho(\bar{U}_i + u_i) dV \\ &+ \int_{CV} \frac{\partial}{\partial x_j} \rho(\bar{U}_i + u_i)(\bar{U}_j + u_j) dV \end{aligned} \quad (3)$$

Applying the Reynolds averaging will result in the following equation:

$$\Sigma(\bar{F}_i) = \frac{\partial}{\partial t} \int_{CV} \rho(\bar{U}_i) dV + \int_{CV} \frac{\partial}{\partial x_j} \rho(\bar{U}_i \bar{U}_j + \overline{u_i u_j}) dV \quad (4)$$

The momentum equation along the x_1 direction, with the effective forces and with the simplifications related to the flow of interest, namely being fully developed, statistically stationary, incompressible, and two-dimensional, is as follows:

$$-\frac{\partial \bar{P}}{\partial x_1} L h w - 2\tau_{12w} L w = \rho \int_{CV} \frac{\partial}{\partial x_2} \overline{u_1 u_2} dV \quad (5)$$

where $\tau_{12w} = \mu \left. \frac{\partial \bar{U}_1}{\partial x_2} \right|_w$ is the viscous shear stress on the lower wall. Using the differential RANS equation, it can be shown that $\overline{u_1 u_2}$ is negative at half the channel height, zero at the wall, and zero at the channel center. Due to the antisymmetry of the Reynolds stress profile about the channel center, the volume integral of the gradient of $\overline{u_1 u_2}$ is zero. Hence, knowing that the pressure gradient is constant in the flow direction, the pressure drop along the CV with length L reads:

$$\Delta P = 2 \frac{L}{h} \underbrace{\mu \left. \frac{\partial \bar{U}_1}{\partial x_2} \right|_w}_{\tau_{12w}} \quad (6)$$

This equation clearly shows that the drop in pressure potential in the flow direction is used to overcome the viscous stresses on the walls. Nevertheless, the effect of turbulence is hidden in the velocity gradient of the mean longitudinal velocity.

The impact of turbulence can be explicitly seen in the transport equation for the mechanical energy, which is

$$\frac{D1/2 U_i U_i}{Dt} = U_i g_i - \frac{1}{\rho} U_i \frac{\partial P}{\partial x_i} + \frac{1}{\rho} U_i \frac{\partial \tau_{ij}}{\partial x_j} \quad (7)$$

All dependent variables in this equation represent instantaneous values. The work done by the viscous forces per unit time (last term) can be rewritten as follows, so that the dissipation rate of mechanical energy becomes visible:

$$\frac{D1/2 U_i U_i}{Dt} = U_i g_i - \frac{1}{\rho} U_i \frac{\partial P}{\partial x_i} + \frac{1}{\rho} \frac{\partial U_i \tau_{ij}}{\partial x_j} - \frac{1}{\rho} \tau_{ij} \frac{\partial U_i}{\partial x_j} \quad (8)$$

$\frac{1}{\rho} \tau_{ij} \frac{\partial U_i}{\partial x_j}$ is the dissipation rate, $\tau_{ij} = \mu(\partial U_i / \partial x_j + \partial U_j / \partial x_i)$ is the viscous stress tensor and g_i is the gravitational acceleration.

For Reynolds averaging, all dependent variables can be decomposed into ensemble mean and fluctuating components as follows:

$$\begin{aligned} U_i &= \bar{U}_i + u_i \\ P &= \bar{P} + p \\ \tau_{ij} &= \bar{\tau}_{ij} + \tau'_{ij} \end{aligned} \quad (9)$$

The overline symbol represents the ensemble averaging. Introducing decomposed variables into Eq. 8 and applying Reynolds Averaging, the ensemble mean of the kinetic energy equation reads:

$$\begin{aligned} &\frac{D1/2 \bar{U}_i \bar{U}_i}{Dt} + \frac{D1/2 \overline{u_i u_i}}{Dt} \\ &+ \overline{u_i u_j} \frac{\partial \bar{U}_i}{\partial x_j} + \bar{U}_i \frac{\partial \overline{u_i u_j}}{\partial x_j} + \frac{1}{2} \frac{\partial \overline{u_i u_i u_j}}{\partial x_j} \\ &= \bar{U}_i g_i - \frac{1}{\rho} \bar{U}_i \frac{\partial \bar{P}}{\partial x_i} - \frac{1}{\rho} \overline{u_i \frac{\partial p}{\partial x_i}} \\ &+ \frac{1}{\rho} \frac{\partial \bar{U}_i \bar{\tau}_{ij}}{\partial x_j} + \frac{1}{\rho} \frac{\partial \overline{u_i \tau'_{ij}}}{\partial x_j} - \frac{1}{\rho} \overline{\tau_{ij}} \frac{\partial \bar{U}_i}{\partial x_j} - \frac{1}{\rho} \overline{\tau'_{ij}} \frac{\partial u_i}{\partial x_j} \end{aligned} \quad (10)$$

Note that $1/2\overline{U_i U_i}$ and $1/2\overline{u_i u_i}$ are the kinetic energy per unit mass of the mean flow and the turbulent flow, respectively. This equation can be split into a mean and a turbulent component. The transport equation for the mechanical energy of the mean flow is:

$$\begin{aligned} & \frac{D1/2\overline{U_i U_i}}{Dt} + \overline{U_i} \frac{\partial \overline{u_i u_j}}{\partial x_j} \\ &= \overline{U_i} g_i - \frac{1}{\rho} \overline{U_i} \frac{\partial \overline{P}}{\partial x_i} + \frac{1}{\rho} \frac{\partial \overline{U_i \tau_{ij}}}{\partial x_j} - \frac{1}{\rho} \overline{\tau_{ij}} \frac{\partial \overline{U_i}}{\partial x_j} \end{aligned} \quad (11)$$

The second term on the left-hand side (LHS) is the extracted energy from the mean by turbulence, and the last term is the dissipation rate of the mean mechanical energy. The transport equation for the turbulent mechanical energy is:

$$\begin{aligned} & \frac{D1/2\overline{u_i u_i}}{Dt} + \overline{u_i u_j} \frac{\partial \overline{U_i}}{\partial x_j} + \frac{1}{2} \frac{\partial \overline{u_i u_i u_j}}{\partial x_j} \\ &= -\frac{1}{\rho} \overline{u_i} \frac{\partial \overline{p}}{\partial x_i} + \frac{1}{\rho} \frac{\partial \overline{u_i \tau'_{ij}}}{\partial x_j} - \frac{1}{\rho} \overline{\tau'_{ij}} \frac{\partial \overline{u_i}}{\partial x_j} \end{aligned} \quad (12)$$

The second and third terms at the LHS are the production of turbulence kinetic energy and the work done by the Reynolds stresses due to turbulent fluctuations, respectively.

The transport equation of mean mechanical energy (8) for the two-dimensional horizontal fully developed incompressible statistically stationary turbulent channel flow simplifies to:

$$\begin{aligned} & \overline{u_i u_j} \frac{\partial \overline{U_i}}{\partial x_j} + \overline{U_i} \frac{\partial \overline{u_i u_j}}{\partial x_j} + \frac{1}{2} \frac{\partial \overline{u_i u_i u_j}}{\partial x_j} \\ &= -\frac{1}{\rho} \overline{U_i} \frac{\partial \overline{P}}{\partial x_i} - \frac{1}{\rho} \overline{u_i} \frac{\partial \overline{p}}{\partial x_i} \\ &+ \frac{1}{\rho} \frac{\partial \overline{U_i \tau_{ij}}}{\partial x_j} + \frac{1}{\rho} \frac{\partial \overline{u_i \tau'_{ij}}}{\partial x_j} - \frac{1}{\rho} \overline{\tau_{ij}} \frac{\partial \overline{U_i}}{\partial x_j} - \frac{1}{\rho} \overline{\tau'_{ij}} \frac{\partial \overline{u_i}}{\partial x_j} \end{aligned} \quad (13)$$

Further simplification can be done when the volume integral of both sides of this equation for the CV in Fig.1 is done. In this integral form, some of the volume integrals can be converted to surface integrals using the divergence theorem. The result of this integration is as follows:

$$\begin{aligned} & \int_{CV} \overline{u_i u_j} \frac{\partial \overline{U_i}}{\partial x_j} dV + \int_{CV} \overline{U_i} \frac{\partial \overline{u_i u_j}}{\partial x_j} dV + \int_{CS} 1/2 \overline{u_i u_i u_j} n_j dA \\ &= -\frac{1}{\rho} \int_{CS} \overline{P} \overline{U_i} n_i dA - \frac{1}{\rho} \int_{CS} \overline{p} \overline{u_i} n_i dA \\ &+ \frac{1}{\rho} \int_{CS} \overline{U_i} \overline{\tau_{ij}} n_j dA + \frac{1}{\rho} \int_{CS} \overline{u_i \tau'_{ij}} n_j dA \\ &- \frac{1}{\rho} \int_{CV} \overline{\tau_{ij}} \frac{\partial \overline{U_i}}{\partial x_j} dV - \frac{1}{\rho} \int_{CV} \overline{\tau'_{ij}} \frac{\partial \overline{u_i}}{\partial x_j} dV \end{aligned} \quad (14)$$

In the derivation for the pressure-related terms, the following continuity equations for the mean and fluctuating

velocities are used:

$$\frac{\partial \overline{U_i}}{\partial x_i} = 0 \quad (15)$$

$$\frac{\partial \overline{u_i}}{\partial x_i} = 0 \quad (16)$$

Because of the no-slip condition and the fully developed state of the flow, the last three surface integrals have to be zero.

$$\begin{aligned} & \int_{CV} \overline{u_i u_j} \frac{\partial \overline{U_i}}{\partial x_j} dV + \int_{CV} \overline{U_i} \frac{\partial \overline{u_i u_j}}{\partial x_j} dV \\ &= -\frac{1}{\rho} \int_{CS} \overline{P} \overline{U_i} n_i dA - \frac{1}{\rho} \int_{CV} \overline{\tau_{ij}} \frac{\partial \overline{U_i}}{\partial x_j} dV - \frac{1}{\rho} \int_{CV} \overline{\tau'_{ij}} \frac{\partial \overline{u_i}}{\partial x_j} dV \end{aligned} \quad (17)$$

The LHS of the above equation represents the sum of turbulence kinetic energy production and the extracted kinetic energy from the mean flow to turbulence. Thus, this sum can be converted to a surface integral, which is also zero owing to fully developed two-dimensional flow:

$$\int_{CV} \overline{u_i u_j} \frac{\partial \overline{U_i}}{\partial x_j} dV + \int_{CV} \overline{U_i} \frac{\partial \overline{u_i u_j}}{\partial x_j} dV = \int_{CS} \overline{U_i u_i u_j} n_j dA = 0 \quad (18)$$

Hence, the production of turbulence kinetic energy is negative of the extracted energy from the mean flow. Hence, Eq. 17 reduces to the balance between the work done by the pressure and the viscous dissipation rate calculated from mean velocity gradients and the gradients of velocity fluctuations, respectively.

$$\int_{CS} \overline{P} \overline{U_i} n_i dA = - \int_{CV} \overline{\tau_{ij}} \frac{\partial \overline{U_i}}{\partial x_j} dV - \int_{CV} \overline{\tau'_{ij}} \frac{\partial \overline{u_i}}{\partial x_j} dV \quad (19)$$

The second term at the right-hand side (RHS) is the dissipation rate of turbulence kinetic energy, i.e., the mass integral of the last term in Eq. 12. Using the divergence theorem and continuity equation for the LHS, and the two-dimensional nature of the flow, this equation can further be simplified to:

$$\int_{CV} \frac{\partial \overline{P}}{\partial x_1} \overline{U_1} dV = - \int_{CV} \overline{\tau_{12}} \frac{\partial \overline{U_1}}{\partial x_2} dV - \int_{CV} \overline{\tau'_{1j}} \frac{\partial \overline{u_1}}{\partial x_j} dV \quad (20)$$

Writing the viscous stress term in terms of mean and fluctuating velocities delivers the final form of the energy balance in integral form as follows:

$$\begin{aligned} \int_{CV} \frac{\partial \overline{P}}{\partial x_1} \overline{U_1} dV &= - \mu \int_{CV} \left(\frac{\partial \overline{U_1}}{\partial x_2} \right)^2 dV \\ &- \mu \int_{CV} \left(\frac{\partial \overline{u_1}}{\partial x_j} \frac{\partial \overline{u_1}}{\partial x_j} + \frac{\partial \overline{u_j}}{\partial x_i} \frac{\partial \overline{u_i}}{\partial x_j} \right) dV \end{aligned} \quad (21)$$

The last term represents the total dissipation rate of turbulence kinetic energy in the CV, and no further simplification can be done for it. When Eq. 21 is carefully

examined, one can end up with the conclusion that the pressure gradient is solely dependent on viscous effects, which is opposite to the observations that the coefficients of pressure drop or drag become independent of viscous effects at high Reynolds numbers [1, 8, 17]. This is a paradox that cannot be explained by Eqn. 21. However, the transport equation of turbulent kinetic energy (12) can resolve it. The integral of this equation for the flow considered here simplifies to

$$\int_{CV} \overline{u_i u_j} \frac{\partial \overline{u_i}}{\partial x_j} dV = -\frac{1}{\rho} \int_{CV} \overline{\tau'_{ij}} \frac{\partial \overline{u_i}}{\partial x_j} dV \quad (22)$$

This equality clearly demonstrates that the production rate of turbulence kinetic energy is precisely counterbalanced by its dissipation rate. Moreover, the causal relationship established in the transport equation asserts that the production rate of turbulence kinetic energy directly dictates its dissipation rate. Hence, the turbulence dissipation rate in Eq. 21 can be replaced by the turbulence kinetic energy production as follows:

$$\int_{CV} \frac{\partial \overline{P}}{\partial x_1} \overline{U_1} dV = -\mu \int_{CV} \left(\frac{\partial \overline{U_1}}{\partial x_2} \right)^2 dV + \rho \int_{CV} \overline{u_1 u_2} \frac{\partial \overline{U_1}}{\partial x_2} dV \quad (23)$$

It is known that $\partial \overline{P} / \partial x_1$ is a constant. Hence, the integral on the LHS becomes

$$\frac{\partial \overline{P}}{\partial x_1} \dot{Q}L = -\mu \int_{CV} \left(\frac{\partial \overline{U_1}}{\partial x_2} \right)^2 dV + \rho \int_{CV} \overline{u_1 u_2} \frac{\partial \overline{U_1}}{\partial x_2} dV \quad (24)$$

where \dot{Q} is the volume flow rate. The resulting relation clearly decomposes viscous and inertial turbulent effects. It reflects how the work done by the pressure gradient is channelled into viscous dissipation and turbulence production rates. This work is transformed irreversibly into internal energy. Furthermore, the viscous and inertial effects contributing to the wall shear stress become visible when $\partial \overline{P} / \partial x_1$ is left alone in this equation and equated to the one obtained from the momentum equation (6) as follows:

$$\tau_{12w} = \frac{\mu h}{2\dot{Q}L} \int_{CV} \left(\frac{\partial \overline{U_1}}{\partial x_2} \right)^2 dV - \frac{\rho h}{2\dot{Q}L} \int_{CV} \overline{u_1 u_2} \frac{\partial \overline{U_1}}{\partial x_2} dV \quad (25)$$

Now, the relation between the wall shear stress, viscous dissipation, and turbulence production becomes apparent. Knowing that the pressure gradient is constant in the flow direction, the pressure drop (Eq. 24) can be written as:

$$\Delta P = \underbrace{\frac{\mu}{\dot{Q}} \int_{CV} \left(\frac{\partial \overline{U_1}}{\partial x_2} \right)^2 dV}_{\Delta P_{visc}} - \underbrace{\frac{\rho}{\dot{Q}} \int_{CV} \overline{u_1 u_2} \frac{\partial \overline{U_1}}{\partial x_2} dV}_{\Delta P_{turb}} \quad (26)$$

This equation is parallel to Colebrook's [1] and Haaland's [3] friction factor relations, which have separate components for viscous and inertial turbulent effects.

B. Order of Magnitude Analysis (OMA)

The equations 6 and 26 can be used to infer the pressure drop's scaling with respect to the other parameters. The former states that the wall shear stress determines the pressure gradient, whereas the latter states that the pressure drop arises due to viscous dissipation of the mean velocity and the production of turbulent kinetic energy.

As the pressure drop equation derived from the energy equation (Eq. 26) explicitly captures the effect of turbulence, it will be used for OMA. At this point, several physically reasonable assumptions have to be made on the representative values of the unknown terms in Eq. 26. The gradients in x_1 and x_2 directions scale with $1/L$ and $1/h$, respectively. $\overline{U_1}$ scales with the ensemble and surface average mean velocity \overline{U}_m , and the $\overline{u_1 u_2}$ scales with the negative of the surface average turbulent kinetic energy, which is $k_m = 0.5(\overline{u_i u_i})$. Hence, the order of magnitudes of each term can be written as follows:

$$\Delta P_{visc} \approx \frac{\mu}{\overline{U}_m h} \int_{CV} \left(\frac{\partial \overline{U_1}}{\partial x_2} \right)_m^2 dV \quad (27)$$

$$\Delta P_{turb} \approx \frac{\rho}{\overline{U}_m h} \int_{CV} k_m \left(\frac{\partial \overline{U_1}}{\partial x_2} \right)_m dV \quad (28)$$

The mean of the absolute value of the mean velocity gradient should reflect the effect of roughness on the change of the velocity profile. Thus, it is approximated by:

$$\left| \frac{\partial \overline{U_1}}{\partial x_2} \right|_m \approx \frac{\overline{U}_m}{h} \left[A + B \left(\frac{\varepsilon}{h} \right)^k \right] \quad (29)$$

where A , B and k are unknown coefficients.

Assuming that the roughness (ε) is the key influencing factor for the level of generated turbulence, the mean turbulence kinetic energy (k_m) and the roughness can be related to each other by a kind of turbulence intensity as follows:

$$\frac{k_m}{\overline{U}_m^2} \approx \left[C + D \left(\frac{\varepsilon}{h} \right)^n \right] \quad (30)$$

Here, a power-law relation is taken with an unknown power n , and C and D are unknown coefficients.

For the same type of flow in a pipe, h can be replaced by the diameter D of the pipe in the above relations. Hence, the orders of magnitude of the pressure drop terms in Eqs. 27 and 28 are:

$$\Delta P_{visc} \approx A_{visc} \frac{\mu \overline{U}_m L}{D} \left[A + B \left(\frac{\varepsilon}{D} \right)^k \right]^2 \quad (31)$$

$$\Delta P_{turb} \approx A_{turb} \rho \overline{U}_m^2 \frac{L}{D} \left[A + B \left(\frac{\varepsilon}{D} \right)^k \right] \times \left[C + D \left(\frac{\varepsilon}{D} \right)^n \right] \quad (32)$$

where A_{visc} and A_{turb} are the correlation constants.

Normalizing this relation with $0.5\rho\bar{U}_m^2 L/D$ results in the following form of friction factor:

$$f_{visc} \approx A_{visc} 2 \frac{1}{Re} \left[A + B \left(\frac{\varepsilon}{D} \right)^k \right]^2 \quad (33)$$

$$f_{turb} \approx A_{turb} 2 \left[A + B \left(\frac{\varepsilon}{D} \right)^k \right] \left[C + D \left(\frac{\varepsilon}{D} \right)^n \right] \quad (34)$$

A first approximation of total pressure drop and corresponding friction factor is the sum of Eqs. 31 and 32. Hence

$$\begin{aligned} \Delta P \approx & A_{visc} \rho \frac{L}{D} \frac{\bar{U}_m}{D} \left[A + B \left(\frac{\varepsilon}{D} \right)^k \right]^2 \\ & + A_{turb} \rho \frac{L}{D} \bar{U}_m^2 \left[C + D \left(\frac{\varepsilon}{D} \right)^n \right] \left[A + B \left(\frac{\varepsilon}{D} \right)^k \right] \end{aligned} \quad (35)$$

$$\begin{aligned} f \approx & A_{visc} 2 \frac{1}{Re} \left[A + B \left(\frac{\varepsilon}{D} \right)^k \right]^2 \\ & + A_{turb} 2 \left[A + B \left(\frac{\varepsilon}{D} \right)^k \right] \left[C + D \left(\frac{\varepsilon}{D} \right)^n \right] \end{aligned} \quad (36)$$

Note that f_{visc} decreases with the Reynolds number and f_{turb} changes only with the roughness as in Haaland's friction factor relation given below:

$$\frac{1}{f^{1/2}} \approx -1.8 \log \left[\frac{6.9}{Re} + \left(\frac{\varepsilon/D}{3.7} \right)^{1.11} \right] \quad (37)$$

The following relations of [7] for ΔP and f hold for a smooth pipe at Reynolds numbers lower than 10^5 .

$$\Delta P \approx 0.158 L \rho^{3/4} \mu^{3/4} D^{-5/4} \bar{U}_m^{7/4} \quad (38)$$

$$f \approx 0.316 Re^{-1/4} \quad (39)$$

Although this ΔP model lacks separate terms for the viscous and turbulent inertial terms, in principle, the power exponent of 7/4 for \bar{U}_m is expected since one can approximate a second-order polynomial, like the one in Eq. 35, by a power function having an exponent between 1 and 2.

The functional forms for the pressure drop and the friction factor (Eqs. 35 and 36) are derived by OMA, but they might not truly represent the exact behaviour. For example, the turbulent part takes a constant value at all Reynolds numbers. However, f becomes Reynolds-number-independent only at large Reynolds numbers. In connection with that, the functional form of f (Eq. 36) is not capable of reproducing the minima for rough pipes, which happens as f transits from the smooth pipe regime to the rough pipe regime. This transition is also Reynolds-number-dependent.

It is important to note that taking the velocity gradient directly proportional to \bar{U}_m/h as shown in Eq. 29 is an assumption. On the contrary, the \bar{U}_m and μ in

Eq. 27, as well as ρ in Eq. 28 are not assumed, i.e., they are part of the derived governing equation. Hence, the power exponents of \bar{U}_m in Eq. 35 can be relaxed, only if the dimensional homogeneity requirement for ΔP model holds. The simplest way to guarantee the dimensional homogeneity is to make a symbolic regression to $f(Re, \varepsilon/D)$ instead of $\Delta P(\bar{U}_m, \rho, \mu, L, D, \varepsilon)$. To have a transition from the smooth pipe regime to a rough pipe regime, the terms in the f equation (36) should be relaxed to reflect the Reynolds number and relative roughness dependencies of this transition. Allowing a transition behavior is legitimate because the assumption that dissipation is determined by production (Eq. 22) is expected to hold for rough pipe flows at high Reynolds numbers. The logistic function has previously been used and can reflect the transition [11]. One form of the logistic function is:

$$g(t) = g_{lower} + \frac{g_{upper} - g_{lower}}{1 + e^{-\beta(t-t_0)}} \quad (40)$$

where t is the independent variable, β is the slope and t_0 is the midpoint of transition. Letting g be f , t be Re , and the upper and lower values to be f_{turb} and f_{visc} of Eqs. 34 and 33, respectively, a more general form of the friction factor can be obtained as follows:

$$\begin{aligned} f & \approx f_{visc} + \frac{f_{turb} - f_{visc}}{1 + e^{-\beta(Re - Re_{tr})}} \\ & = f_{visc} \frac{e^{-\beta(Re - Re_{tr})}}{1 + e^{-\beta(Re - Re_{tr})}} + f_{turb} \frac{1}{1 + e^{-\beta(Re - Re_{tr})}} \end{aligned} \quad (41)$$

$Re_{tr}(\varepsilon/D)$ is the midpoint of transition and $\beta(\varepsilon/D)$ is the slope of the transition. These parameters are functions of relative roughness, and $\beta(\varepsilon/D)$ is expected to rise with increasing ε/D , whereas $Re_{tr}(\varepsilon/D)$ is expected to decrease. For the curve fitting, $Re_{tr}(\varepsilon/D) = Q/(\varepsilon/D)^r$ and $\beta = S(\varepsilon/D)^p$ can be used with the coefficients Q , r , S , and p . After relaxing the exponent of Re from one to η , the functional form of the friction factor equation can be written as:

$$\begin{aligned} f \approx & \frac{2A_{visc}}{Re^\eta} \left[A + B \left(\frac{\varepsilon}{D} \right)^k \right]^2 \frac{e^{-S(\varepsilon/D)^p [Re - Q/(\varepsilon/D)^r]}}{1 + e^{-S(\varepsilon/D)^p [Re - Q/(\varepsilon/D)^r]}} \\ & + A_{turb} 2 \left[A + B \left(\frac{\varepsilon}{D} \right)^k \right] \frac{[C + D \left(\frac{\varepsilon}{D} \right)^n]}{1 + e^{-S(\varepsilon/D)^p [Re - Q/(\varepsilon/D)^r]}} \end{aligned} \quad (42)$$

This functional form with 13 coefficients is used to fit a nonlinear curve (Fig. 2) to the low-Reynolds-number data of [8], the high-Reynolds-number data of [18], and the high-Reynolds-number data of [19]. The constants of the curve fit are given in Table I. The fit in Fig. 2 is very accurate up to $Re = 10^6$, but it can not catch the high Reynolds number behavior of the smooth pipe as Colebrook's relation.

The resulting ΔP can be obtained simply multiplying the equation above by $L/D 0.5\rho\bar{U}_m^2$ as follows:

TABLE I: Curve-fit coefficients of Eq. 42.

Coefficient	Value	Coefficient	Value
A_{visc}	0.8825	k	0.4
A_{turb}	0.6632	n	0.5299
η	0.2233	S	0.003263
A	0.5294	Q	44.11
B	0.006	p	1.303
C	0.03556	r	0.844
D	0.8237	—	—

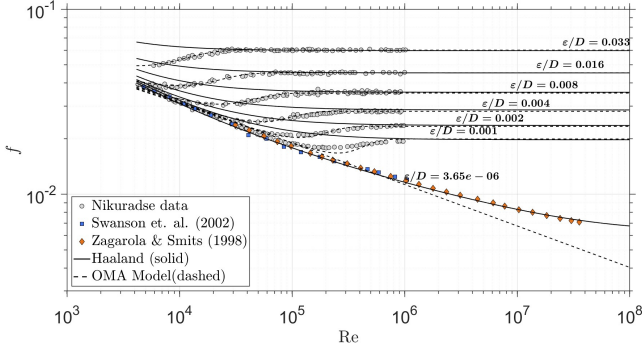


FIG. 2: OMA-based nonlinear regression to Eq. 43.

$$\begin{aligned}
 \Delta P = & A_{visc} \rho^{1-\eta} \mu^\eta \frac{L}{D} \frac{\bar{U}_m^{2-\eta}}{D^\eta} \left[A + B \left(\frac{\varepsilon}{D} \right)^k \right]^2 \\
 & \times \frac{e^{-\beta(Re-Re_{tr})}}{1 + e^{-\beta(Re-Re_{tr})}} \\
 & + A_{turb} \rho \frac{L}{D} \bar{U}_m^2 \left[A + B \left(\frac{\varepsilon}{D} \right)^k \right] \frac{[C + D \left(\frac{\varepsilon}{D} \right)^n]}{1 + e^{-\beta(Re-Re_{tr})}}
 \end{aligned} \quad (43)$$

It is not surprising to see that for $\eta = 0.2233$, the exponents of OMA-based equations converge to those of Blasius in Eqs. 38 and 39 for smooth pipes.

C. Constraints for Regression

Despite their complexity and the extensive number of unknown parameters in Eqs. 41 and 43, it is better to use these equations to guide symbolic regression alongside the experimental data. To bias the search toward physically admissible regressions for f , we incorporate four constraints (C_1 - C_4), which are implemented in the regression process by using lightweight and model-only diagnostics to verify their fulfilment. These diagnostics are evaluated on synthetic grids of the independent variables. Using the friction factor regression models, the pressure drop is calculated over the synthetic grid, and the constraints are checked for fulfilment. The constraints are derived as follows:

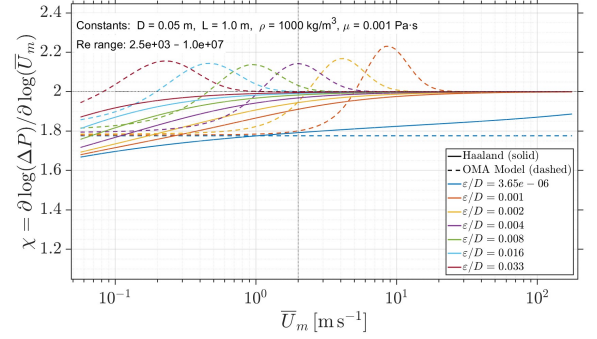


FIG. 3: Exponent of surface average mean velocity of OMA-based model and Haaland's model.

1. Constraint C_1 : Velocity Sensitivity Exponent

According to Eqs. 42 and 43, the dependence of ΔP on the mean speed \bar{U}_m at fixed $\rho, \mu, \varepsilon, D$, and L is a linear-plus-quadratic superposition. At sufficiently small \bar{U}_m the viscous term dominates and $\Delta P \propto \bar{U}_m$; at sufficiently large \bar{U}_m the turbulent term dominates and $\Delta P \propto \bar{U}_m^2$. We cannot control the exact shape of the SR model during regression, but locally, it can be approximated by a power law

$$\Delta P_{\text{model}} \approx R \bar{U}_m^\chi. \quad (44)$$

A local logarithmic velocity exponent χ is then defined as

$$\chi = \frac{\partial \log \Delta P_{\text{model}}}{\partial \log \bar{U}_m} = \frac{\bar{U}_m}{\Delta P_{\text{model}}} \frac{\partial \Delta P_{\text{model}}}{\partial \bar{U}_m}. \quad (45)$$

Evaluating χ for the OMA model over the Nikuradse data range shows that it smoothly interpolates between $\chi \approx 1$ in the viscous limit and values slightly above $\chi = 2$ in the smooth-rough transition, before relaxing back toward $\chi = 2$ in the fully rough regime. In particular, the OMA model remains within $1 \lesssim \chi \lesssim \chi_{\text{max}}$ with $\chi_{\text{max}} \simeq 2.4$. We therefore use the following properties as constraint C_1 :

$$\Delta P_{\text{model}} \text{ is non-decreasing in } \bar{U}_m, \quad (46a)$$

$$1 \lesssim \chi \lesssim \chi_{\text{max}}, \quad (46b)$$

$$\lim_{\bar{U}_m \rightarrow \infty} \chi = 2. \quad (46c)$$

Here χ_{max} is taken directly from the OMA prediction; it is used as a soft upper bound during regression rather than a hard universal limit.

2. Constraint C_2 : Sensitivity to Roughness at Fixed Reynolds Number

In the OMA model (Eq. 42), wall roughness enters only through increasing factors of the form $(\varepsilon/D)^k$ and

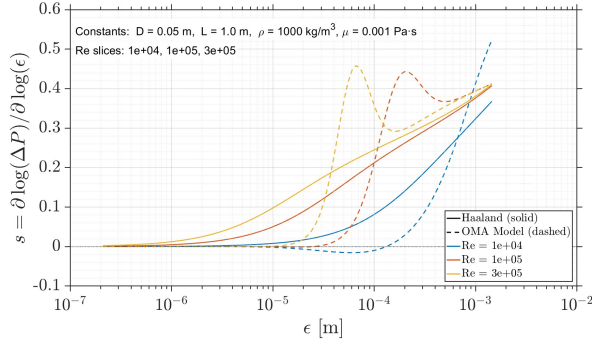


FIG. 4: Exponent of roughness of OMA-based model and Haaland's model.

$(\varepsilon/D)^n$ with $k, n \geq 0$. At fixed $\bar{U}_m, \rho, \mu, D, L$ this implies that the pressure drop must not *systematically* decrease when the pipe is made rougher: Once the flow is in the hydraulically rough regime, additional roughness can only increase the resistance. We quantify the roughness sensitivity through the logarithmic exponent:

$$s = \frac{\partial \log \Delta P}{\partial \log \varepsilon} = \frac{\varepsilon}{\Delta P} \frac{\partial \Delta P}{\partial \varepsilon}. \quad (47)$$

When evaluated on the OMA model over Nikuradse-like conditions, s is non-negative and remains below a modest upper bound $s_{\max} \approx 0.4$. This motivates the following testable properties at fixed Reynolds number:

$$\frac{\partial \Delta P}{\partial \varepsilon} \geq 0, \quad (48a)$$

$$0 \leq s = \frac{\partial \log \Delta P}{\partial \log \varepsilon} \lesssim s_{\max} \approx 0.4. \quad (48b)$$

Small, localized negative values of s near the hydraulically smooth limit are interpreted as numerical artifacts of the finite-difference evaluation and are tolerated to a limited extent. The precise aggregation of violations into a scalar C_2 score is described in the constraint-scoring section.

3. Constraint C_3 : Viscous Consistency at Fixed Velocity

At fixed \bar{U}_m, ρ, D, L the OMA model contains a viscous contribution that is linear in μ and a turbulent contribution that does not depend explicitly on μ . In the hydraulically smooth regime, this yields a small positive logarithmic exponent, whereas in the fully rough regime, the pressure drop becomes effectively independent of μ . We measure this with:

$$\alpha = \frac{\partial \log \Delta P}{\partial \log \mu} = \frac{\mu}{\Delta P} \frac{\partial \Delta P}{\partial \mu}. \quad (49)$$

For the OMA model, α lies in a narrow positive range $0 \lesssim \alpha \lesssim 0.3$ and approaches $\alpha \rightarrow 0$ as $\varepsilon/D \rightarrow \infty$. The

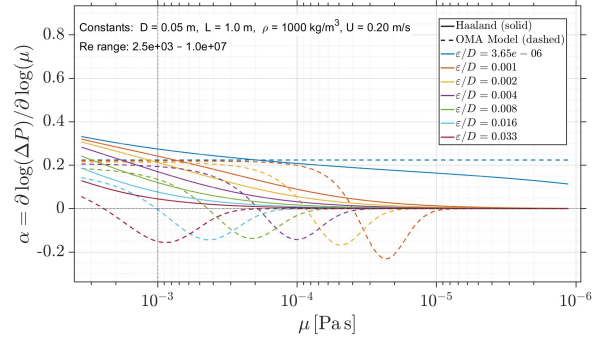


FIG. 5: Exponent of viscosity of OMA-based model and Haaland's model.

SR equation preserves the same qualitative trend, but can show mildly negative α for very rough pipes and low Reynolds numbers, where the explicit roughness dependence dominates and increasing μ shifts the operating point along a nearly flat portion of the rough plateau. Guided by the OMA envelope, we therefore adopt:

$$\alpha_{\min} \leq \alpha \leq \alpha_{\max}, \quad (50a)$$

$$\lim_{Re \rightarrow \infty} \alpha = 0, \quad (50b)$$

with $\alpha_{\min} \approx -0.5$ and $\alpha_{\max} \approx 1$. These values are wide enough to contain the SR model wherever it matches the OMA behaviour, while excluding unphysical strong decreases or increases of ΔP with viscosity.

4. Constraint C_4 : Density Sensitivity at Fixed Velocity

In the OMA model, at fixed \bar{U}_m, μ, D, L the turbulent contribution is linear in ρ whereas the viscous term is independent of ρ . Neglecting the weak density-dependence of the friction factor, this suggests a logarithmic exponent of order unity:

$$\gamma = \frac{\partial \log \Delta P}{\partial \log \rho} = \frac{\rho}{\Delta P} \frac{\partial \Delta P}{\partial \rho}. \quad (51)$$

When evaluated on the OMA model over the turbulent range, γ stays close to one, typically $0.7 \lesssim \gamma \lesssim 1$, and approaches $\gamma \rightarrow 1$ as the flow becomes fully rough. The SR correlation reproduces this structure but, in the smooth-rough transition, the implicit ρ -dependence through Re can reinforce the explicit ρ factor and yield exponents up to $\gamma \approx 1.3$. Using OMA as the physical reference, we thus relax the upper bound while enforcing positivity of $\partial \Delta P / \partial \rho$:

$$0 \leq \gamma \leq \gamma_{\max}, \quad (52a)$$

$$\frac{\partial \Delta P}{\partial \rho} \geq 0, \quad (52b)$$

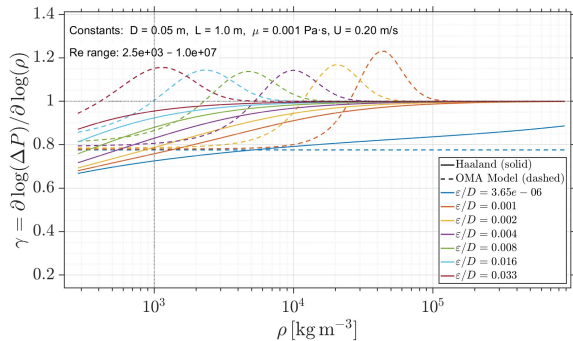


FIG. 6: Exponent of density of OMA-based model and Haaland’s model.

with $\gamma_{\max} \approx 1.4$. This keeps the effective density exponent in the OMA-consistent order-unity range while preventing any unphysical decrease of pressure drop with increasing density.

D. Symbolic Regression with Constraints

We implement symbolic regression by modifying the multi-gene genetic programming framework of GPTIPS 2.0 [16]. The most obvious modifications are the conversion from 2-D to 3-D optimization and the new joint coefficient optimization method. Each individual model is a linear combination of G expression trees (genes):

$$f(\text{Re}, \varepsilon/D) = \sum_{g=1}^G w_g T_g(\text{Re}, \varepsilon/D; \theta_g),$$

where each gene T_g is built from a primitive set $\{+, -, \times, /, (\cdot)^m, \log, \exp, \tanh\}$, terminal nodes are dimensionless inputs from the Buckingham–II grid, and θ_g collects ephemeral (numeric) constants inside the trees.

Population initialization. The initial population is generated by ramped half-and-half with prescribed depth and node limits. Domain-safe primitives (protected division, safe logarithms, etc.) are used so that every expression can be evaluated on the entire training grid $(\text{Re}, \varepsilon/D)$ without producing non-finite values.

Joint optimization of weights and constants. For each individual, all numeric quantities that can be tuned are collected into a single parameter vector

$$\text{par} = (w_1, \dots, w_G, \theta_1, \dots, \theta_G).$$

Optimization proceeds in two stages. First, with constants θ_g fixed at their current values, all genes are evaluated on the training set to form a design matrix G whose columns contain the gene outputs. A ridge regression on G provides an initial estimate of the weights w_g ; any non-finite columns are zeroed so that pathological genes are

automatically assigned zero weight. Second, the warm-started weights are concatenated with the current constants to form an initial vector par_0 , and a Nelder–Mead search is applied to minimize the prediction error of ΔP on the training data. Unlike standard GPTIPS 2, this step jointly refines both linear coefficients and non-linear constants, which helps prevent extremely nested functions while improving asymptotic behaviour and agreement with Nikuradse trends.

Three objective components. In our modified version of GPTIPS 2.0, using the optimized parameter vector par^* , each individual is evaluated in terms of three minimization objectives:

- **Fitness** J_{err} : root-mean-squared error (RMSE) of the predicted ΔP on the training set.
- **Complexity** J_{comp} : the total number of nodes (operators, variables, and constants) in the final symbolic expression. Since our models are multi-gene, we compute J_{comp} by summing the node counts of all gene trees. In this paper, this value is reported simply as “nodes”.
- **Physics objective** J_{phys} : we compute the four constraint scores C_1 – C_4 from the order-of-magnitude analysis (velocity exponent, roughness monotonicity, viscous consistency, density sensitivity). Each $C_k \in [0, 1]$ measures violation of the corresponding OMA trend, and we aggregate them as

$$J_{\text{phys}} = \max\{C_1, C_2, C_3, C_4\},$$

so that a model is only considered strongly physics-consistent if it behaves correctly in all four directions.

This yields a three-dimensional objective vector

$$\mathbf{J} = (J_{\text{fit}}, J_{\text{comp}}, J_{\text{phys}})$$

Numerical evaluation of the physics scores. For any candidate friction-factor model $f_{\text{model}}(\text{Re}, \varepsilon/D)$, we evaluate it as a pressure-drop predictor via

$$\Delta P_{\text{model}} = f_{\text{model}}(\text{Re}, \varepsilon/D) \frac{\rho \bar{U}_m^2 L}{2D},$$

Constraint scores are computed from logarithmic derivatives estimated using finite-difference or gradient operators on log-spaced grids; any non-finite or non-positive model output encountered during a sweep is treated as a hard failure and yields the maximal penalty for that sweep.

Score C_1 enforces velocity-scaling consistency. For each tested ε/D , we sweep $\text{Re} \in [10^4, 10^9]$ on a log grid (160 points), map to $\bar{U}_m = \text{Re} \mu_{\text{ref}} / (\rho D)$, and estimate

$$\chi = \frac{\partial \log \Delta P_{\text{model}}}{\partial \log \bar{U}_m}$$

using **gradient** applied to $\log \Delta P$ versus $\log \bar{U}_m$ (after a light three-point moving-average smoothing). We apply a two-zone envelope: in the transitional range $10^4 \leq Re \leq 10^6$ we require $1.0 \leq \chi \leq 2.4$, while in the fully rough tail $10^6 \leq Re \leq 10^9$ we enforce $\chi \approx 2$ within tolerance $\text{tolB} = 0.01$. The two penalties are combined as $0.3 \text{penA} + 0.7 \text{penB}$ per roughness level, and C_1 is taken as the worst case over ε/D .

Score C_2 enforces roughness monotonicity. At 12 Reynolds-number slices $Re \in [3 \times 10^3, 10^8]$, we sweep the physical roughness ε on a log grid (360 points) spanning: $\varepsilon \in [0.5(\varepsilon/D)_{\min} D, 1.5(\varepsilon/D)_{\max} D]$ and compute

$$s = \frac{\partial \log \Delta P_{\text{model}}}{\partial \log \varepsilon}$$

using **gradient**. We tolerate small negative slopes via $s \geq -s_{\text{allow}}$ with $s_{\text{allow}} = 0.1$, and define C_2 by combining the fraction of violating grid points across ε and then averaging across Reynolds slices.

Score C_3 enforces viscosity consistency. At fixed $\varepsilon/D = 10^{-3}$ we sweep $\mu \in [10^{-4}, 10^{-1}]$ (120 log-spaced points) while keeping $\bar{U}_m = 2 \text{m/s}$ by setting $Re = \rho \bar{U}_m D / \mu$. We then compute $\Delta P_{\text{model}}(\mu)$ and set C_3 to the fraction of points where ΔP decreases with increasing μ (zero tolerance in the current implementation).

$$\alpha = \frac{\partial \log \Delta P_{\text{model}}}{\partial \log \mu}$$

Score C_4 enforces density consistency. At fixed $\varepsilon/D = 10^{-3}$ and $\bar{U}_m = 2 \text{m/s}$ we sweep $\rho \in [10^2, 10^4]$ (20 log-spaced points) and estimate

$$\gamma = \frac{\partial \log \Delta P_{\text{model}}}{\partial \log \rho}$$

We take $C_4 = \langle |\gamma - 1| \rangle$, with invalid evaluations assigned $C_4 = 1$. The overall physics objective is reported as $J_{\text{phys}} = \max(C_1, C_2, C_3, C_4)$.

Finally, the overall physics objective reported in the Pareto analysis is

$$J_{\text{phys}} = \max(C_1, C_2, C_3, C_4),$$

so that any strong violation in one channel dominates the physics score.

3-D Pareto selection. We use Pareto dominance and crowding distance in the three dimensional objective space ($J_{\text{err}}, J_{\text{comp}}, J_{\text{phys}}$): individuals are ranked into Pareto fronts, crowding distance promotes coverage of the trade-off surface, and tournament selection favours non-dominated individuals with large crowding distance while maintaining predictive pressure toward low J_{err} . Crucially, J_{phys} is not folded into the fitness as a weighted penalty; treating physics as an independent axis avoids arbitrary weighting and yields cleaner trade-off.

Variation, elitism and termination. From the selected parents, crossover, mutation, and direct reproduction are applied with prescribed probabilities to form the

next generation; a small elite subset of the current Pareto front is copied unchanged. After a fixed number of generations, the final 3-D Pareto front is exported, and candidate correlations are chosen by inspecting the trade-off between fitness, complexity, and physicality within the constraints.

III. RESULTS

A. Pareto Trade-off

The multi-objective search produces a final population evaluated by three criteria: the data fitness J_{err} , the structural complexity J_{comp} (node count), and the physics score

$J_{\text{phys}} = \max(C_1, \dots, C_4)$, where smaller values are preferable in all objectives. Rather than visualizing the outcome in a three dimensional scatter space, we report the results as objective values versus population index and as robustness summaries for selected candidates. Each point corresponds to one symbolic individual after convergence of the multi-objective GP run; lower values are preferable in all three coordinates. Blue markers denote all individuals, while red markers indicate the non-dominated subset (Pareto front). This representation makes it easier to identify clusters of high-performing solutions and to locate specific candidates by index, while revealing the expected trade-off: individuals with very low J_{err} often require higher complexity J_{comp} or exhibit weaker physics compliance (larger J_{phys}), whereas strongly physics-compatible solutions typically sacrifice some predictive accuracy. From the Pareto set we selected four representative candidates (Table II), spanning different compromises among error, complexity, and physics score. Two different runs, namely run A and run B, are examined to extract candidate equations. Run B has a stricter constraint check procedure compared to Run A.

Candidate 1 (index 714) given in Eq. 53 offers the best pure data fit and very good physics compliance, at the cost of being the most complex. As seen in Fig. 9, its dashed curves track the Nikuradse and smooth-pipe data closely across all roughness levels and reproduce the smooth-rough transition with realistic curvature.

$$\begin{aligned} f_1 = & 0.2544 \frac{\varepsilon}{D} + 0.1663 \left(\frac{\varepsilon}{D} \right)^{\left(\frac{1}{Re(\varepsilon/D)^{0.9736}} + 0.9937 \right)^{118.2}} \\ & + 0.033 \left(0.1026 \frac{\varepsilon}{D} - \frac{32840 \frac{\varepsilon}{D} - 2159}{Re} \right)^{0.4667} \\ & - 0.027 \left[\frac{\varepsilon}{D} + \frac{1}{Re} \left(\frac{1}{Re(\varepsilon/D)^{1.1}} + 84.17 \right) \right]^{-0.029} \\ & + 0.046 \end{aligned} \tag{53}$$

Candidate 2 given in Eq. 54 represents a different cor-

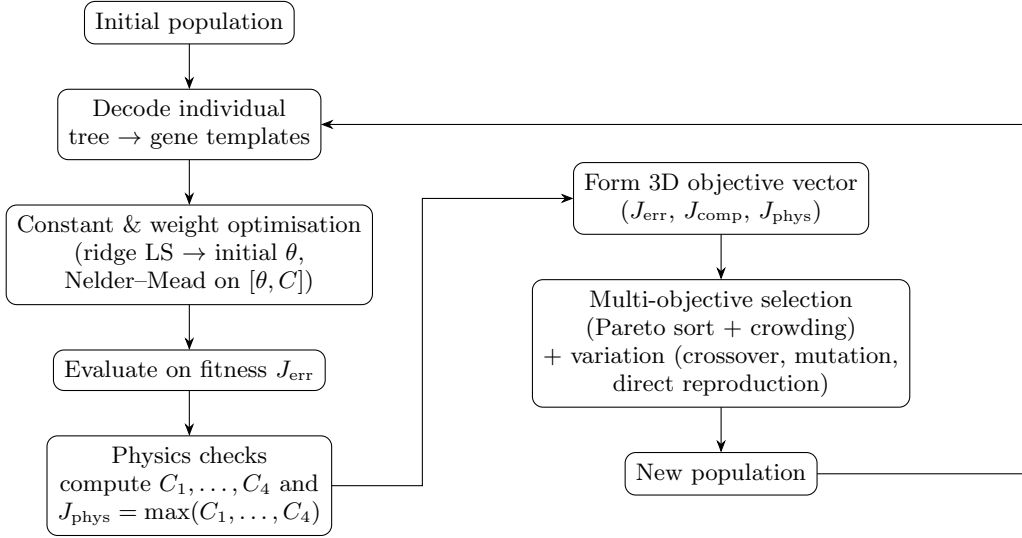


FIG. 7: Workflow of the symbolic regression with physics constraints: each individual undergoes joint optimisation of gene weights and constants, physics checks C_1 – C_4 , and 3D Pareto selection on $(J_{\text{err}}, J_{\text{comp}}, J_{\text{phys}})$ over successive generations.

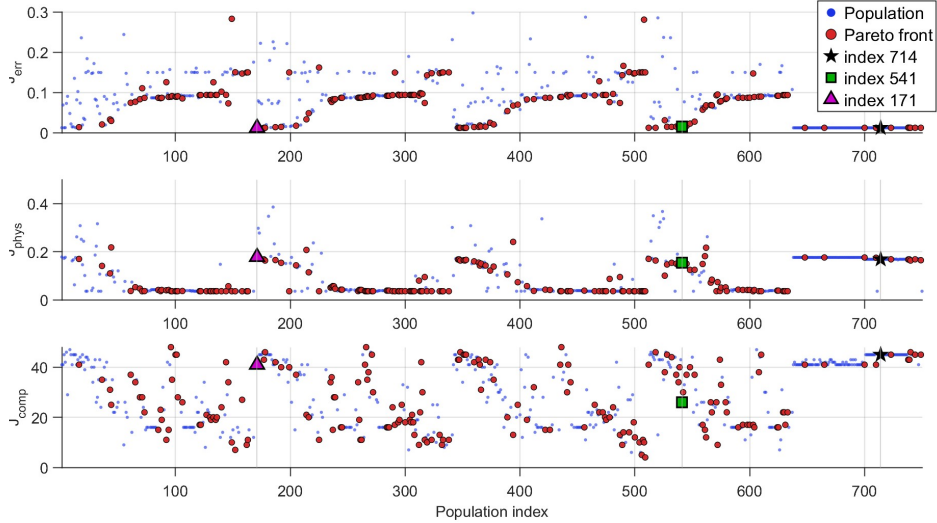


FIG. 8: Objective function results over indices for Run A.

ner of the Pareto front: it is substantially simpler (26 nodes) and has the best physics scores ($J_{\text{phys}} \approx 0.15$), but their training errors are about 25% larger than Candidate 1. In the Moody-style plot, it reproduces the overall structure correctly, but the smooth branch shows a slightly different slope at high Re , and the rough plateau sits a little below the Nikuradse data for some ε/D . These deviations are acceptable from a purely physical standpoint but lead to visibly larger residuals. The cor-

relation of Candidate 2 is:

$$\begin{aligned}
 f_2 = & 0.23 \frac{\varepsilon}{D} + 0.12 \left(\frac{\varepsilon}{D} \right) \left(\frac{1}{Re(\varepsilon/D)^{0.89} + 1} \right)^{220} \\
 & + 0.062 \left(0.22 \frac{\varepsilon}{D} + \frac{\varepsilon/D + 440}{Re} \right)^{0.28} + 4.6 \times 10^{-3}.
 \end{aligned} \tag{54}$$

Candidate 3 given in Eq. 55 has a similar analytical structure to Candidate 1 (Eq. (53)) but with slightly different exponents and numerical constants. It achieves almost the same error with somewhat lower complexity (41 nodes) at the price of a slightly larger physics score, mainly due to more pronounced deviations in the C_2 and C_3 envelopes. On the Moody-style plot, the rough-

TABLE II: Selected symbolic regression candidates on the $(J_{\text{err}}, J_{\text{comp}}, J_{\text{phys}})$ Pareto front. Candidate 4 is taken from a different run, since that run used a tighter tolerance instead of the standard value in the C_1 computation; we re-evaluated its J_{phys} using the standard settings for a fair comparison.

Candidate	Run	Index	J_{err}	J_{phys}	J_{comp}	Role
1	A	714	0.0121	0.168	45	Best fitness
2	A	541	0.0153	0.154	26	Simple
3	A	171	0.0126	0.178	41	Trade-off
4	B	639	0.0123	0.161	45	Tighter tolerance result
Haaland	–	–	0.1230	0.155	–	Baseline correlation

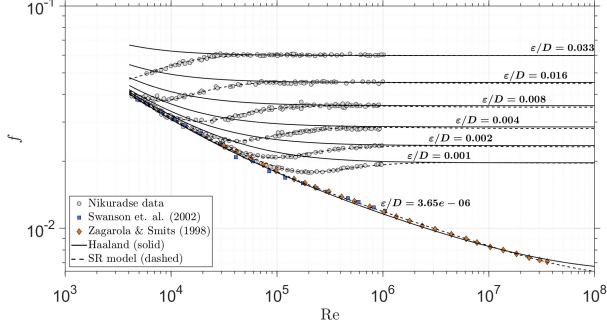


FIG. 9: Nikuradse’s friction factor with predetermined dimensionless numbers for Candidate 1 (Re , relative roughness)

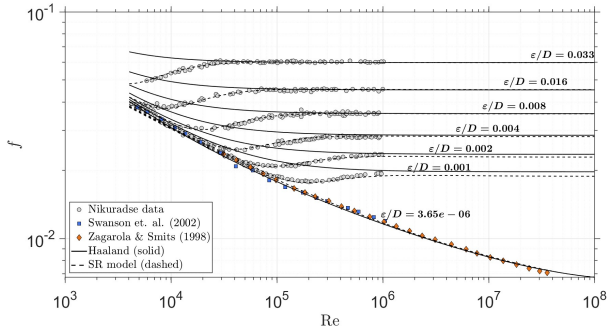


FIG. 10: Nikuradse’s friction factor with predetermined dimensionless numbers for Candidate 2 (Re , relative roughness).

branch regions are marginally less flat than for Candidate 1, and the transition for $\epsilon/D \approx 10^{-3}$ is shifted. The

correlation of Candidate 3 is:

$$\begin{aligned}
 f_3 = & 0.25 \frac{\epsilon}{D} - 0.035 \left[\frac{\epsilon}{D} + \frac{1}{Re} \left(\frac{1}{(\epsilon/D)^{1.1}} + 110 \right) \right]^{-0.029} \\
 & + 0.17 \left(\frac{\epsilon}{D} \right)^{\left(\frac{1}{Re (\epsilon/D)^{0.98}} + 0.99 \right)^{110}} \\
 & + 0.04 \left(0.0013 - \frac{2.1 \times 10^4 \frac{\epsilon}{D} - 1.5 \times 10^3}{Re} \right)^{0.48} \\
 & + 0.055
 \end{aligned} \tag{55}$$

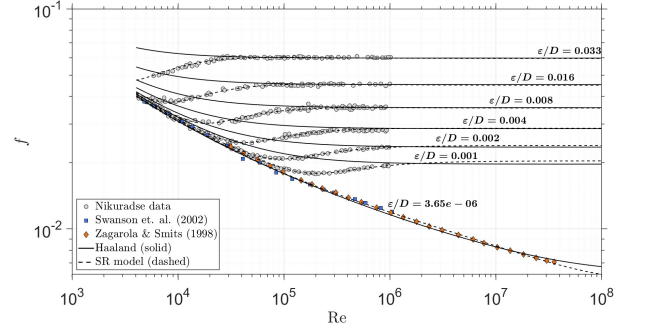


FIG. 11: Nikuradse’s friction factor with predetermined dimensionless numbers for Candidate 3 (Re , relative roughness).

Candidate 4 (from a separate run) given in Eq. 56 attains a training error comparable to the best models ($J_{\text{err}} \approx 0.0123$) with similar complexity (45 nodes), while keeping a competitive physics score ($J_{\text{phys}} \approx 0.161$). Its structure differs noticeably from Candidates 1–3: instead of a single dominant power-law/exponent-gated roughness term, it combines (i) a smooth activation term in Re through $\tanh(32950/Re + 1.38)$, (ii) a weak power-law correction in $(\cdot)^{0.1584}$, and (iii) two Reynolds-dependent “switch” factors of the form $(a/x_2)^{c/Re} = \exp((c/Re) \ln(a/x_2))$. These exponential-like factors are close to unity at high Re but can noticeably modulate the prediction at moderate Re , providing additional flexibility in the smooth–rough transition. The explicit viscous correction $-27.38/Re$ further helps shape the smooth-branch behaviour. Overall, Candidate 4 can be viewed as a viable alternative that matches the Nikuradse trends

well with similar complexity; we therefore retain it as a strong contender pending further validation. The correlation of Candidate 4 is:

$$\begin{aligned}
f_4 = & 0.319 \frac{\varepsilon}{D} - 0.0345 \tanh\left(\frac{32950}{Re} + 1.38\right) \\
& + 0.1316 \left[\left(\frac{\varepsilon}{D}\right)^2 - \frac{178.2(\varepsilon/D) - 22260/Re}{Re} \right]^{0.1584} \\
& - 0.034 \left(\frac{0.3391}{\varepsilon/D}\right)^{-11940/Re} \\
& + 0.035 \left(\frac{0.1135}{\varepsilon/D}\right)^{-13930/Re} - \frac{27.38}{Re} + 0.03416
\end{aligned} \tag{56}$$

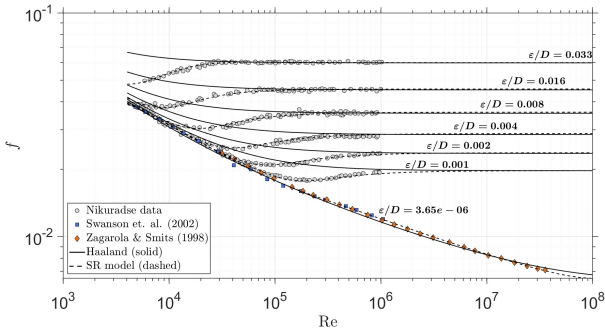


FIG. 12: Nikuradse’s friction factor with predetermined dimensionless numbers for Candidate 4(Re , relative roughness).

After observing the Pareto results, Candidate-1 was selected as the primary model for future analyses.

B. Physical Interpretation of Candidate 1

For interpretation it is convenient to group the four nonlinear terms in Candidate 1 (Eq. (53)):

$$T_1 = 0.2544 \frac{\varepsilon}{D} \tag{57a}$$

$$T_2 = 0.1663 \left(\frac{\varepsilon}{D}\right)^{\left(\frac{1}{Re(\varepsilon/D)^{0.9736}} + 0.9937\right)^{118.2}} \tag{57b}$$

$$T_3 = 0.033 \left(0.1026 \frac{\varepsilon}{D} - \frac{32840(\varepsilon/D) - 2159}{Re}\right)^{0.4667} \tag{57c}$$

$$T_4 = -0.027 \left[\frac{\varepsilon}{D} + \frac{1}{Re} \left(\frac{1}{Re(\varepsilon/D)^{1.1}} + 84.17\right)\right]^{-0.029} \tag{57d}$$

For clarity, we analyse only the four nonlinear contributions T_1 - T_4 ; the additive bias in Eq. (53) is a constant offset and does not affect the regime structure.

The term structure is not arbitrary: it mirrors the canonical decomposition of pipe friction into a smooth-wall Reynolds-number dependence, a rough-wall plateau, and a rapid smooth rough crossover familiar from the Moody Diagram, Nikuradse’s sand-grain data, and Colebrook-type interpolation. Below we interpret each term in this context, drawing connections to modern high- Re friction laws and to outer-layer similarity ideas often used to rationalize rough-wall scaling.

1. Term T_1 : Fully Rough Wall Contribution

The leading explicit roughness term $T_1 = 0.2544(\varepsilon/D)$ supplies the dominant fully rough scaling. In the limit $Re \rightarrow \infty$ at fixed ε/D , the friction factor effectively independent of Re , producing the well-known horizontal plateaux of Moody diagram. This behaviour is experimental signature of the fully rough regime mapped by Nikuradse and later embedded in Colebrook-White: once viscosity no longer controls the near-wall stress, drag is set primarily by relative roughness. In the perspective of outer-layer similarity, roughness introduces a geometric length scale that replaces the viscous scale in setting the wall stress, so the leading dependence is on ε/D rather than on Re . Candidate 1 enforces this physics explicitly through T_1 , yielding (for high Re):

$$f_1 \approx 0.2544 \frac{\varepsilon}{D} + (\text{subdominant corrections}) \tag{58}$$

Although classical fully-rough laws are often written in logarithmic form (e.g. via a roughness function shift in the log law, and thus a log dependence on ε when expressed as $1/\sqrt{f}$), over the moderate roughness range represented in Nikuradse/Superpipe-style datasets an approximately linear leading-order dependence of f on ε/D can act as an effective surrogate; here T_1 provides precisely that leading roughness sensitivity.

2. Term T_2 : Roughness Onset Gate

The most distinctive feature of Candidate 1 is the highly nonlinear term T_2 , which activates roughness dependence only beyond a threshold in $(Re, \varepsilon/D)$. By defining

$$z(Re, \varepsilon/D) = \left(0.9937 + \frac{1}{Re(\varepsilon/D)^{0.9736}}\right)^{118.2}, \tag{59}$$

We have $T_2 = 0.1663(\varepsilon/D)^z$. This makes clear that the large exponent 118.2 does not represent a new physical power law; it acts as a steepness parameter for a smooth blending function. Mathematically, a large outer power turns a modest change in the base into an abrupt change in z so T_2 behaves like a quasi-step activation (a ’soft Heaviside’), analogous in effect to using a logistic

or *tanh*-type switch with a large slope to blend between smooth and rough asymptotes. Candidate 1 makes the switching mechanism explicit in an algebraic form.

Because the outer exponent 118.2 makes z extremely sensitive when the base crosses unity, we define an onset Reynolds number ' Re_{on} ' and set the base in (59) to unity, giving

$$Re_{\text{on}}(\varepsilon/D) \approx \frac{1}{(1 - 0.9937)(\varepsilon/D)^{0.9736}} \approx \frac{1.59 \times 10^2}{(\varepsilon/D)^{0.9736}} \quad (60)$$

For $Re \lesssim Re_{\text{on}}$, the base exceeds unity so z grows rapidly; since $\varepsilon/D < 1$, $(\varepsilon/D)^z$ collapses and T_2 is effectively inactive, consistent with a hydraulically smooth response in which roughness elements are submerged within the viscous-affected near-wall region. For $Re \gg Re_{\text{on}}$, the base approaches 0.9937 and z saturates to a moderate value $z \approx (0.9937)^{118.2} \approx 0.47$, so $(\varepsilon/D)^z$ is no longer vanishingly small and T_2 contributes at $O(\varepsilon/D^{0.47})$. In this sense, T_2 provides an explicit and interpretable analogue of the smooth to rough crossover embedded in Colebrook-type formulas: it introduces a sharp transition band in Re whose location scales approximately as $Re_{\text{on}} \propto (\varepsilon/D)^{-1}$, consistent with the classical notion that transition is governed by a roughness Reynolds Number (roughness size measured in wall units) reaching $O(1)$ to $O(10^2)$.

3. Term T_3 : Smooth Wall Reynolds Number Dependence

The term T_3 carries the principal Reynolds-number dependence of Candidate 1 when ε/D is small (hydraulically smooth) or when roughness has not yet been activated by T_2 . In the limit $\varepsilon/D \rightarrow 0$, $T_1 \rightarrow 0$ and T_2 is strongly suppressed, so the model reduces primarily to the Re -dependent structure in T_3 (with a weak correction from T_4). The explicit appearance of $1/Re$ inside the base raised to a fractional power (0.4667) gives T_3 enough flexibility to reproduce the observed curvature of the smooth friction curve: a relatively rapid decrease at moderate Re that progressively weakens at higher Re as the flow approaches the logarithmic asymptote. This interpretation is aligned with high- Re smooth-pipe measurements from the Princeton Superpipe, a facility developed to access very large Re_D and thereby assess friction-factor relations and their associated universal constants over an extended range of Reynolds number. In particular, McKeon *et al.* [20], using Superpipe friction data up to $Re_D = 3.5 \times 10^7$, showed that the constants in Prandtl's universal friction relation are accurate only over a limited Reynolds-number range and become increasingly biased at higher Re_D , motivating revised constants grounded in a logarithmic-overlap description of the mean velocity profile. In Candidate 1, T_3 plays the analogous role: it supplies the smooth-wall backbone that captures finite- Re curvature across the combined Nikuradse/Superpipe

parameter range before roughness contributions (T_1 - T_2) become active.

4. Term T_4 : Weak Interaction Correction

The remaining term T_4 is deliberately weak: its exponent is -0.029 , so

$$x^{-0.029} = \exp(-0.029 \ln x) \approx 1 - 0.029 \ln x,$$

i.e. T_4 provides a near-logarithmic correction over wide ranges of x . Accordingly, T_4 does not determine the leading asymptotic behaviour; instead it fine-tunes the intermediate curvature and the quantitative matching between the smooth-wall trend (dominated by T_3) and the roughness-controlled plateau (anchored by T_1 , with transition shaped by T_2). The mixed dependence in the bracket of T_4 combines ε/D and $1/Re$ in a way that naturally produces small, smooth shifts across the transition without introducing non-physical inflections. From an engineering-correlation perspective, T_4 plays the role of a gentle "shape corrector" that can adjust the depth/curvature of the Colebrook-like shape transition while preserving the correct limits as $Re \rightarrow \infty$ and/or $\varepsilon/D \rightarrow 0$.

5. Synthesis and Implications

Candidate 1 can therefore be read as an explicit composite correlation that recovers the standard three-part structure of turbulent pipe friction. Term T_3 provides a Superpipe-consistent smooth-wall dependence on Re ; term T_1 anchors an Re -independent roughness-controlled plateau; term T_2 supplies a sharp but continuous activation of roughness effects, mathematically analogous to a steep logistic/*tanh* blending function and consistent with the narrow smooth-rough crossover observed in Nikuradse data; and term T_4 adds a weak, nearly log-like interaction correction that improves quantitative curvature without altering the asymptotic regime structure. This decomposition addresses the common interpretability concern associated with large exponents and small coefficients: the large exponent in T_2 primarily controls switch sharpness, while the small exponent in T_4 produces a gentle corrective adjustment. Taken together, the four terms constitute a compact explicit representation of the classical picture encoded implicitly by Colebrook-White and refined by modern high- Re measurements: smooth-wall decay with increasing Re , an abrupt transition band whose location scales approximately as $(\varepsilon/D)^{-1}$, and an Re -independent fully rough tail governed primarily by ε/D .

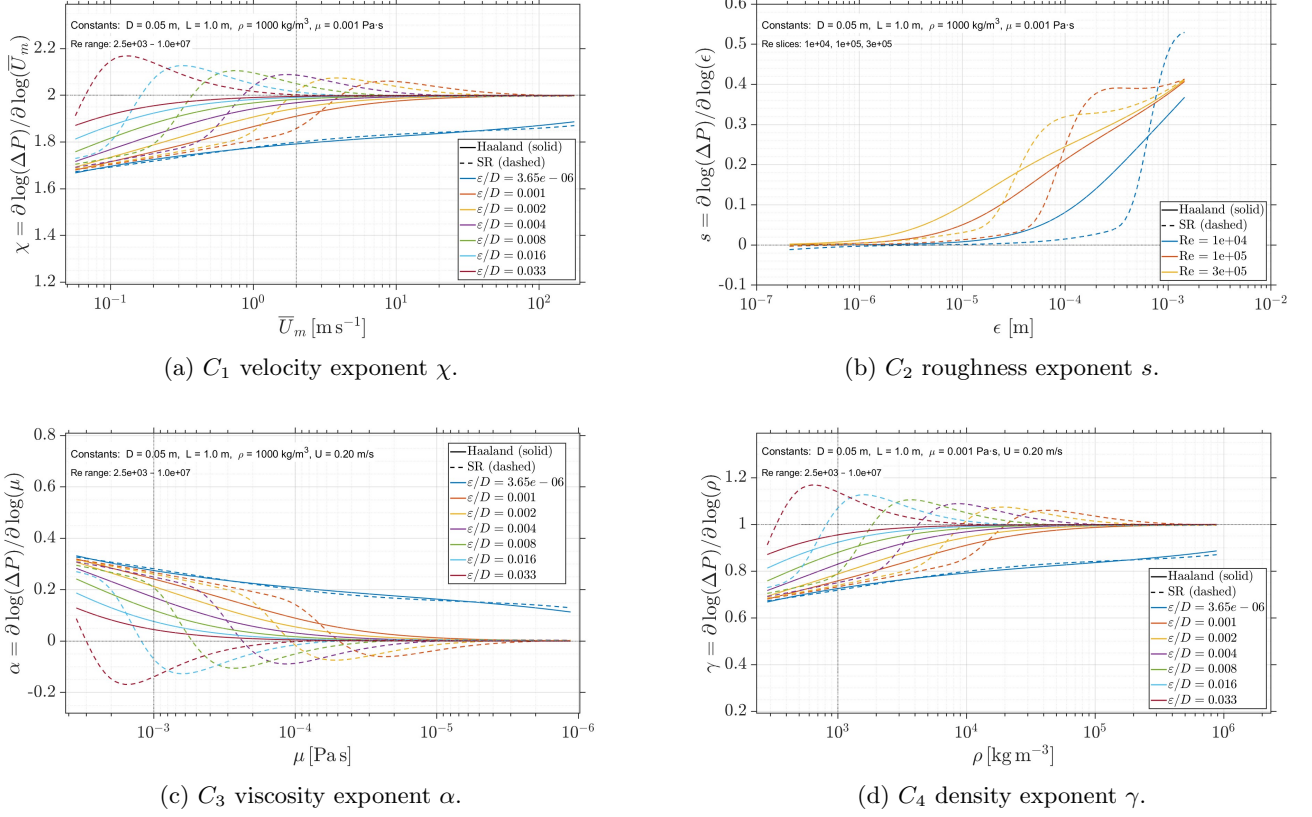


FIG. 13: Constraint checks for Candidate 1 (Eq. (53)), evaluated over the same parameter ranges as the OMA reference. Panels (a)–(d) correspond to C_1 – C_4 , respectively.

C. Constraint behaviour of Candidate 1

Figures 13a–13d show the four constraint checks for Candidate 1 (Eq. (53)), evaluated in the same parameter ranges as for the OMA reference. Here χ , s , α , and γ denote the local logarithmic exponents of ΔP with respect to \bar{U}_m , ε , μ , and ρ , respectively.

C_1 (velocity exponent χ). In Fig. 13a, the dashed curves for Candidate 1 stay close to the OMA envelope: for all tested roughness values and across $Re \in [2.5 \times 10^3, 10^6]$, the velocity exponent lies between about 1.7 and 2.2 and approaches 2 toward the high- Re end. This behaviour follows directly from Eq. (53): in the smooth regime the residual $1/Re$ -like dependence inherited from T_3 produces an effective exponent slightly below 2, whereas in the rough regime the nearly constant plateau $f \approx 0.25 \varepsilon/D$ forces $\Delta P \propto \rho \bar{U}_m^2$ so that $\chi \rightarrow 2$. The slight increase in χ near the smooth–rough transition indicates finite- Re interaction between T_2 and T_3 . However, the curves remain within the OMA-based admissible band, resulting in a low C_1 score.

C_2 (roughness exponent s at fixed Re). Figure 13b shows $s = \partial \log \Delta P / \partial \log \varepsilon$ at Reynolds-number slices in the turbulent regime. For each slice, the dashed curves increase monotonically with ε and remain non-negative,

so the model respects the requirement that ΔP should not decrease when the wall becomes rougher. At very small ε/D the exponent s stays close to zero, consistent with the dominance of the smooth $1/Re$ term in Eq. (53). As ε/D enters the transition range, the activation of T_2 and the growing linear term T_1 cause s to rise toward values around 0.3–0.4, matching the OMA envelope and the curvature of the Nikuradse rough branches. The steeper rise of the dashed curves relative to Haaland reflects that Eq. (53) contains an explicit ε/D prefactor (through T_1), whereas the Haaland correlation embeds roughness more implicitly in the logarithm.

C_3 (viscosity exponent α at fixed \bar{U}_m). In Fig. 13c the dashed curves show how $\alpha = d \log \Delta P / d \log \mu$ varies with μ for several roughness levels at a fixed bulk velocity. For small ε/D and moderate Re the model behaves as expected from the OMA decomposition: $\alpha \approx 0.3$, reflecting a mix of viscous and turbulent contributions. As μ decreases (so Re increases), the combinations $1/(Re(\varepsilon/D)^p)$ in T_2 and T_4 decay and the rough plateau term T_1 dominates. In this limit, the friction factor becomes nearly independent of μ , and $\alpha \rightarrow 0$. The small negative excursions of α visible for the roughest pipes arise when the $1/Re$ -dependent part of T_3 overcompensates the fading viscous contribution; these are confined

to high- Re , rough conditions where the OMA model itself predicts a very weak μ -sensitivity.

C_4 (density exponent γ at fixed \bar{U}_m). Finally, Fig. 13d reports $\gamma = d \log \Delta P / d \log \rho$. Because $f_{(1)}$ depends on ρ only through Re , increasing ρ at fixed \bar{U}_m, μ both multiplies ΔP by ρ and drives Re upward. In the smooth regime the $1/Re$ contribution counteracts part of the explicit ρ factor, leading to $\gamma < 1$; in the fully rough regime the Re -dependence is negligible and $\Delta P \propto \rho \bar{U}_m^2$, so $\gamma \rightarrow 1$. The dashed curves in Fig. 13d follow exactly this pattern: they rise monotonically with ρ , stay positive, and asymptote to a value close to one, in good agreement with the OMA envelope. This yields a low C_4 score while allowing subtle deviations from Haaland in the intermediate range where the data exhibit some scatter.

Overall, the constraint curves of Candidate 1 remain close to the OMA-based envelopes in all four projections while tracking the Nikuradse-like transitions more faithfully than the Haaland correlation.

The candidate models presented above employ only the four base physical constraints of Section IIC, which enforce regime-consistent scaling without restricting the internal mathematical structure. A consequence of this flexibility is that the optimization can produce exponents of order $\mathcal{O}(10)^2$, as seen, e.g., in Eq. 53. Although such values exceed what traditional engineering practice typically considers comfortable, where exponents of order unity are preferred, they arise here to achieve sharp but continuous regime transitions.

Additional constraints based, e.g. on engineering experience, can be incorporated to suppress large exponents. However, a single correlation with fixed exponents cannot be expected to represent vastly different operating conditions, such as high-density turbulent liquid-metal flows versus low-density flows at supercritical pressure and temperature conditions. The aim of this work is therefore to provide a robust framework that can be adapted for specific cases of engineering interest.

D. Validation on rough Superpipe datasets

A final check of the learned correlation is performed on rough-pipe measurements from the Princeton/Oregon "Superpipe" facility. In addition to the smooth-pipe datasets of Swanson *et al.* [18] (Oregon) and Zagarola *et al.* [21] (Princeton), which were already included in the training set, we consider two rough-pipe campaigns that were not used for training: the sand-blasted pipe of [22], and the honed pipe of [23]. These four datasets span the effective roughness ratios of

$\varepsilon/D \approx 7.6 \times 10^{-6}$ (Swanson *et al.*), 3.4×10^{-6} (Zagarola & Smits), 5.9×10^{-5} (Shockling *et al.*), and 6.2×10^{-5} (Langelandsvik *et al.*), all at Reynolds numbers up to $Re \sim 10^7$. The latter two cases therefore provide an out-of-sample test in roughness: their ε/D values are almost

an order of magnitude larger than the Nikuradse sand-grain pipes used during training.

Figure 14 compares these four datasets with the Haaland correlation and with the symbolic regression of Candidate 1. For the two nearly smooth Superpipe smooth Superpipe datasets (Swanson [18] and Zagarola *et al.* [21]) the SR curve follows the data almost indistinguishably from Haaland across the whole turbulent range, confirming that the learned correlation preserves the classical $\Delta P \propto Re^{-0.25}$ behaviour in the hydraulically smooth regime and smoothly connects to the laminar-turbulent transition already demonstrated in the Nikuradse-based Moody plot.

For the rough Shockling [22] and Langelandsvik [23] pipes, the situation is more demanding. Here, the SR model is required to extrapolate in ε/D beyond the Nikuradse training range while retaining the correct asymptotic region $f \sim \text{const}(\varepsilon/D)$ at very large Re . In Fig. 14, the SR prediction (dashed) and Haaland (solid) both capture the overall level and weak Reynolds-number dependence of the data, with the Candidate 1 curve lying between the two rough datasets over most of the range. Systematic deviations are visible in the fully rough region, where the SR model slightly underestimates the Shockling/Langelandsvik friction factors at the highest Reynolds numbers. This discrepancy is comparable in magnitude to the mismatch between Haaland and the same data, and likely reflects a combination of uncertainties in the effective roughness height of the Superpipe inserts and the known differences between Nikuradse's uniform sand-grain roughness and the machined surfaces used in the Superpipe facility. Overall, the Superpipe validation indicates that the physics-informed SR model generalizes reasonably well to roughness levels that were not present in the training set. It preserves the desired smooth-pipe asymptotics and the correct trend toward a roughness-controlled plateau, while exhibiting deviations in the extreme rough regime that are similar to those of the widely used Haaland approximation. This suggests that the combination of dimensional analysis, order-of-magnitude-based constraints, and multi-objective symbolic regression produces a friction-factor correlation that is both interpretable when applied to independent high- Re rough-pipe experiments.

E. Robustness of Symbolic Candidates

To evaluate how robust each candidate equation is against variations in regression coefficients, we apply a perturbation of $\pm 1\%$ (uniform, multiplicative noise) and reassess the model response. Here, the goal is instead to probe how sensitive each discovered functional form is to small changes in its fitted constants—a practical proxy for the identifiability and numerical conditioning of the learned symbolic mechanisms.

We evaluate robustness of all Candidate equations at three representative ($Re, \varepsilon/D$) points chosen to span dis-

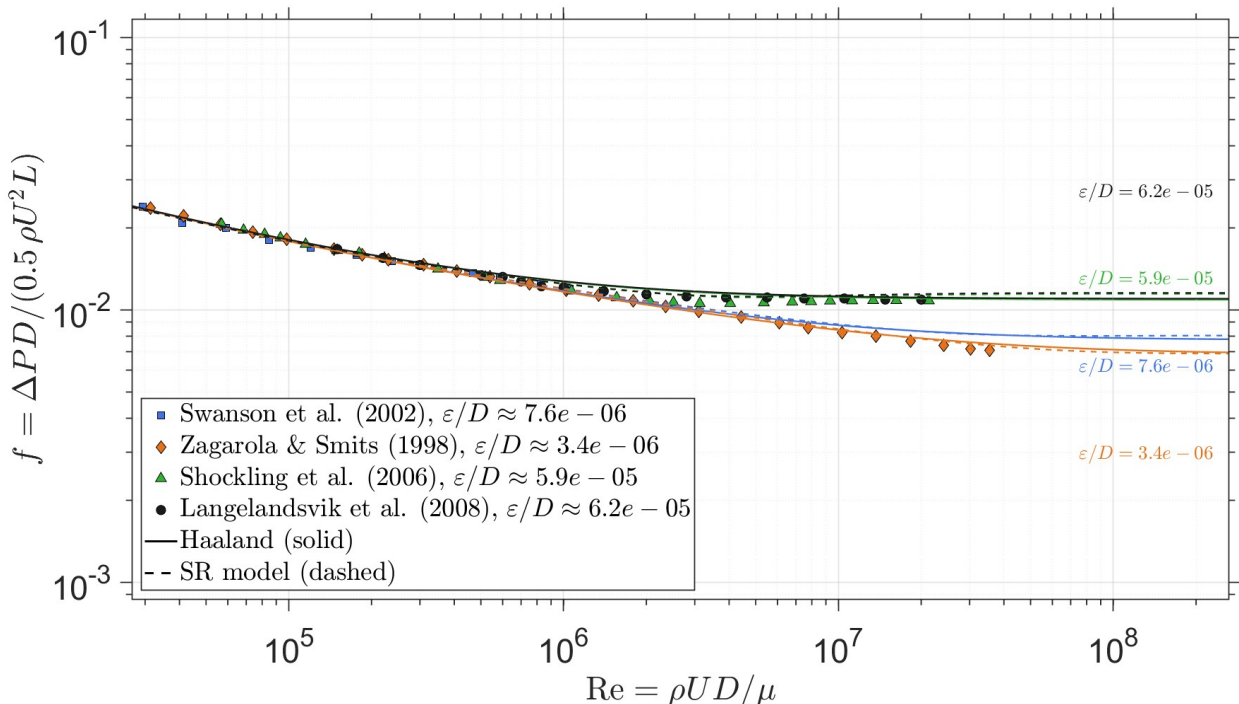


FIG. 14: Independent high- Re validation of friction-factor predictions for rough pipes. Experimental data (markers) are shown for four nominal ε/D levels (see legend); the Haaland correlation (solid) and the SR model (dashed) are overlaid. The SR model reproduces the observed trends from $Re \sim 10^5$ to 10^8 across both low-roughness and fully rough-leaning cases, demonstrating generalization beyond the training set.

tinct regimes of the Moody map: a hydraulically smooth case (small ε/D), a fully rough case (large ε/D at high Re), and an intermediate/transitional case (moderate Re at appreciable roughness). This regime-based selection helps distinguish regression candidates that are globally stable from those that are only locally stable in certain regions of $(Re, \varepsilon/D)$ space. For each trial, we compute the signed deviation of J_{err} and J_{err} relative to the nominal (unperturbed) prediction at the same operating point. Those deviations are defined as

$$\Delta J_{\text{err}} = (f_{\text{dev}} - f_{\text{nom}})/f_{\text{nom}} \quad (61)$$

$$\Delta J_{\text{phys}} = J_{\text{phys,dev}} - J_{\text{phys,nom}} \quad (62)$$

The distributions of deviations at three different points are shown in Fig. 15 for Candidate 1. The physics-score deviations are more difficult to interpret directly because J_{phys} is assembled via non-smooth operations (e.g. maxima over constraint components and clipping). As a result, small coefficient changes can trigger *constraint switching* (changes in the active C_k) or move a point across a tolerance boundary, producing asymmetric and sometimes discontinuous changes in J_{phys} . This explains why ΔJ_{phys} can appear non-Gaussian or even bimodal in Fig. 15, and motivates quantile-based summaries rather than variance-only measures when reporting robustness.

We summarize the central 95% interval of the signed prediction deviation ΔJ_{err} and the corresponding change

in physics score ΔJ_{phys} in Fig. 16a and b, respectively. Black tick marks in those figures indicate the sample median. Haaland exhibits a clear deterioration at the transitional point (Point 3), consistent with the fact that a smooth implicit correlation is not tuned to local constraint envelopes in that regime. Candidate 4 is comparatively well-behaved under coefficient noise: its intervals remain narrow at all three points, and its medians stay close to zero, indicating that its mechanisms respond smoothly to small constant variations. Candidates 1–3 show markedly wider tails, i.e. occasional large excursions despite medians remaining near zero. This sensitivity is consistent with sharp “gating” substructures (large outer exponents and threshold-like factors), where small coefficient changes can shift an internal transition boundary and produce amplified changes at specific $(Re, \varepsilon/D)$ locations. In that sense, the sensitivity is not purely a defect: it reflects high confidence in a narrow transition band, while the median behaviour indicates typical robustness away from rare boundary shifts.

IV. CONCLUSION

This work introduced an order-of-magnitude (OMA) and data-based, physics-informed symbolic regression framework to discover compact friction-factor correla-

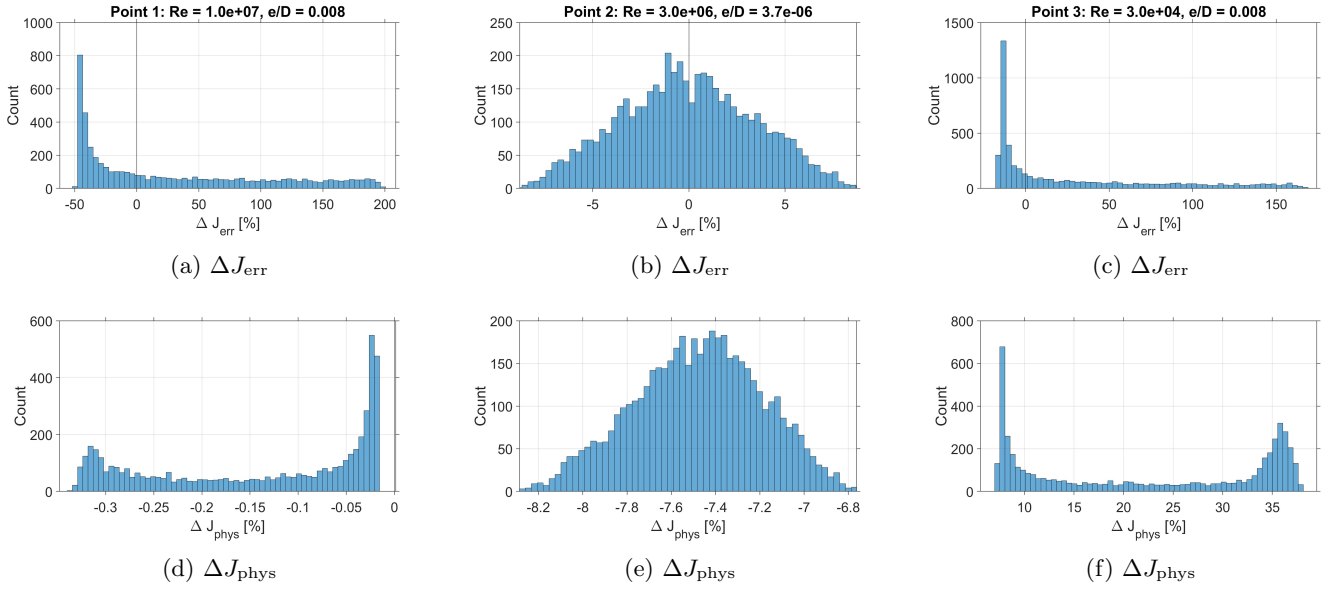


FIG. 15: Histograms of the deviation of J_{err} and J_{phys} from the optimized point corresponding to 1% deviation of the constants of symbolic regression show the robustness of the equation Candidate 1.

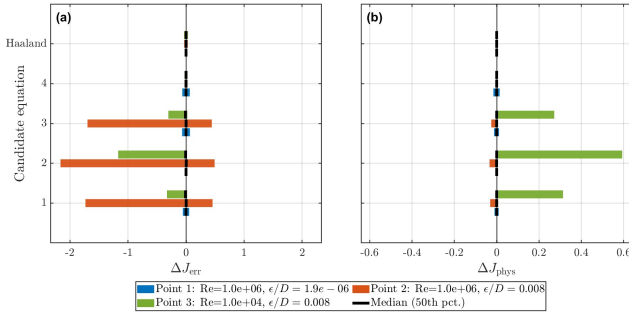


FIG. 16: Robustness test on four different candidates in terms of deviation of (a) friction factor (ΔJ_{err}) and (b) deviation of constraint score (ΔJ_{phys}). The central 95% interval of the signed deviations are shown. Black tick marks in those figures indicate the sample median.

tions across turbulent pipe-flow regimes. By combining classical similarity ideas [5, 6] with multiobjective genetic programming [12, 16], the approach searches directly for explicit algebraic models that balance predictive accuracy, structural simplicity, and physics-based regime/envelope requirements.

Unlike conventional single-objective curve fitting and many data-only symbolic regression studies, our formulation (i) enforces physical constraints spanning the smooth, transitionally rough, and fully rough behaviors and (ii) treats model selection as a Pareto decision rather than a single "best-fit" outcome. This perspective is particularly relevant for rough-pipe friction, where the canonical experimental and engineering references highlight distinct regimes and nontrivial transition behavior

[1–3, 8, 22, 23].

A central contribution of the study is that the OMA is not used merely as qualitative intuition, but as a constructive model scaffold. Starting from the momentum/energy balance, the pressure drop is decomposed into viscous and turbulence-associated contributions, which motivates a friction-factor structure containing a Reynolds-number-decaying component and a roughness-controlled component. To capture the transition minimum, we smoothly blend the viscous and turbulent limits using a ε/D , Re -dependent switch. This OMA-based approach provides two practical benefits: it yields an interpretable baseline correlation and, more importantly, it supplies quantitative envelope expectations for sensitivity exponents (C_1 – C_4), which become lightweight, model-only constraints that guide symbolic regression toward regime-consistent behavior.

A second contribution is a robustness characterization targeting the discovered equations themselves. Rather than perturbing physical inputs, we perturb the fitted regression coefficients to probe numerical conditioning and sensitivity of the symbolic structure—an important practical consideration when models contain sharp non-linear "gating" mechanisms. The resulting robustness summaries complement regime-wise physical interpretations and help distinguish between models that are accurate but brittle and those that remain stable under small coefficient uncertainty.

Finally, beyond reproducing the training datasets, we validated the correlation learned in independent rough Superpipe campaigns that were not used for training [22, 23]. These delicate cases provide an out-of-sample test in ε/D at very high Reynolds numbers, where the model must extrapolate in roughness while preserving

the correct smooth-pipe asymptotics and the trend toward a roughness-controlled plateau. The symbolic correlation generalizes reasonably to these conditions, with deviations in the extreme rough tail comparable to those of widely used explicit engineering approximations [3]. This validation supports the broader claim that combining OMA guidance with multiobjective physics-informed SR can produce correlations that are both interpretable and practically transferable.

Overall, the results show that physics-guided multiobjective symbolic regression can recover interpretable, deployable friction-factor correlations that remain consistent with classical pipe-flow datasets and correlations across regimes, while providing an explicit trade-off surface for accuracy–simplicity–physics compliance. In particular, the framework offers a pathway for extending friction-factor predictions to extreme thermal-hydraulic environments, such as liquid metal-cooled nuclear reactors, supercritical water systems, and corroded high-temperature industrial equipment and components, where standard correlations like Haaland’s, calibrated primarily from conventional air and water data, may require refinement or replacement. The methodology is general and can be ported to other dimensionless-correlation problems where regime structure and asymptotics are known but flexible functional forms are desired.

ACKNOWLEDGMENTS

This study was supported by the Scientific and Technological Research Council of Türkiye (TÜBİTAK), Project No:123M535 and by the EU co-funded part-

nership CONNECT-NM under Grant Agreement No. 101165375. The authors sincerely thank Prof. Dr. Dr. h.c. Franz Durst and Prof. Dr. El-Sayed Zanoun for the valuable discussion.

DATA AVAILABILITY STATEMENT

Collected and combined data and symbolic regression programs are available at GitHub:
https://github.com/emreunal13/GPTIPS2.0_OMAPISR

DECLARATION OF INTERESTS

The authors report no conflict of interest.

AUTHOR CONTRIBUTION STATEMENT

Yunus Emre Ünal: Conceptualization, Methodology, Software, Investigation, Visualization, Data curation, Validation, Writing – original draft, Writing – review & editing;

Özgür Ertunç: Conceptualization, Methodology, Data curation, Supervision, Project administration, Funding acquisition, Writing – original draft, Writing – review & editing;

İsmail Arı: Methodology, Validation, Funding, Writing – review & editing;

Ivan Otić: Conceptualization, Methodology, Formal Analysis, Funding, Writing – review & editing.

-
- [1] C. F. Colebrook, Turbulent flow in pipes, with particular reference to the transition region between the smooth and rough pipe laws, *Journal of the Institution of Civil Engineers* **11**, 133 (1939).
- [2] L. F. Moody, Friction factors for pipe flow, *Transactions of the ASME* **66**, 671 (1944).
- [3] S. E. Haaland, Simple and explicit formulas for the friction factor in turbulent pipe flow, *Journal of Fluids Engineering* **105**, 89 (1983).
- [4] F. M. White, *Viscous Fluid Flow*, 3rd ed. (McGraw–Hill, 2006).
- [5] E. Buckingham, On physically similar systems; illustrations of the use of dimensional equations, *Physical Review* **4**, 345 (1914).
- [6] P. W. Bridgman, *Dimensional Analysis* (Yale University Press, 1922).
- [7] H. Blasius, Das Ähnlichkeitsgesetz bei reibungsvorgängen in flüssigkeiten, *Forschungsheft des Vereins Deutscher Ingenieure* **131**, 1 (1913).
- [8] J. Nikuradse, *Laws of Flow in Rough Pipes*, Tech. Rep. (National Advisory Committee for Aeronautics, 1950) english translation of VDI Forschungsheft 361 (1933).
- [9] C. Colebrook, *Experiments with Fluid Friction in Roughened Pipes*, Tech. Rep. (Imperial College, 1937).
- [10] D. A. Strickler and W. M. Keck, *Translation T-10 Contributions to the Question of a Velocity Formula and Roughness Data for Streams, Channels and Closed Pipelines*, Tech. Rep. (California Institute of Technology, 1981).
- [11] K. S. Yang and D. D. Joseph, Virtual nikuradse, *Journal of Turbulence* **10**, 1 (2009).
- [12] J. R. Koza, *Genetic Programming: On the Programming of Computers by Means of Natural Selection* (MIT Press, 1992).
- [13] M. Schmidt and H. Lipson, Distilling free-form natural laws from experimental data, *Science* **324**, 81 (2009).
- [14] S.-M. Udrescu and M. Tegmark, Ai feynman: a physics-inspired method for symbolic regression, *Science Advances* **6**, eaay2631 (2020).
- [15] M. Cranmer, A. Sanchez-Gonzalez, P. Battaglia, R. Xu, K. Cranmer, D. Spergel, and S. Ho, Discovering symbolic models from deep learning with inductive biases, in *Advances in Neural Information Processing Systems*, Vol. 33 (2020) pp. 17429–17442.
- [16] D. P. Searson, Gptips 2: An open-source software platform for symbolic data mining, in *Handbook of Genetic*

- Programming Applications* (Springer International Publishing, 2015) pp. 551–573.
- [17] I. E. Idelchik, *Handbook of Hydraulic Resistance* (Jaico Publishing House, 2005).
- [18] C. J. Swanson, B. Julian, G. G. Ihas, and R. J. Donnelly, Pipe flow measurements over a wide range of reynolds numbers using liquid helium and various gases, *Journal of Fluid Mechanics* **461**, 51 (2002).
- [19] A. J. Smits and M. V. Zagarola, Response to “scaling of the intermediate region in wall-bounded turbulence: The power law” [phys. fluids 10 , 1043 (1998)], *Physics of Fluids* **10**, 1045 (1998).
- [20] B. J. McKeon, M. V. Zagarola, and A. J. Smits, A new friction factor relationship for fully developed pipe flow, *Journal of Fluid Mechanics* **538**, 429 (2005).
- [21] M. V. Zagarola and A. J. Smits, Mean-flow scaling of turbulent pipe flow, *Journal of Fluid Mechanics* **373**, 33 (1998).
- [22] M. A. Shockling, J. J. Allen, and A. J. Smits, Roughness effects in turbulent pipe flow, *Journal of Fluid Mechanics* **564**, 267 (2006).
- [23] L. I. Langelandsvik, G. J. Kunkel, and A. J. Smits, Flow in a commercial steel pipe, *Journal of Fluid Mechanics* **595**, 323 (2008).